Applied Catalysis B: Environmental 243 (2019) 522–536

Contents lists available at ScienceDirect

Applied Catalysis B: Environmental

journal homepage: www.elsevier.com/locate/apcatb

High rate CO_2 photoreduction using flame annealed TiO_2 nanotubes

Piyush Kar[a,*], Sheng Zeng[a], Yun Zhang[a], Ehsan Vahidzadeh[a], Ajay Manuel[a], Ryan Kisslinger[a], Kazi M. Alam[a], Ujwal K. Thakur[a], Najia Mahdi[a], Pawan Kumar[a,*], Karthik Shankar[a,b,*]

[a] Department of Electrical and Computer Engineering, University of Alberta, Edmonton, Alberta T6G 2V4, Canada
[b] National Institute for Nanotechnology, National Research Council Canada, Edmonton, Alberta T6G 2M9, Canada

ARTICLE INFO

Keywords:
Solar fuel
Carbon dioxide photoreduction
Mass spectrometry
FTIR
Semiconductor
Photocatalysis
FDTD simulations

ABSTRACT

The photocatalytic reduction of CO_2 into light hydrocarbons using sunlight and water is a challenging reaction involving eight electron transfer steps; nevertheless, it has great potential to address the problem of rising anthropogenic carbon emissions and enable the use of fossil fuels in a sustainable way. Several decades after its first use, TiO_2 remains one of the best performing and most durable photocatalysts for CO_2 reduction albeit with a poor visible light absorption capacity. We have used flame annealing to improve the response of TiO_2 to visible photons and engineered a nanotubular morphology with square-shaped cross-sections in flame-annealed nanotubes. An enhanced CH_4 yield was achieved in the photoreduction of CO_2 using flame annealed TiO_2 nanotubes, and isotope labeled experiments confirmed the reaction products to originate from the CO_2 reactant. Flame-annealed TiO_2 nanotubes formed in aqueous electrolyte (FANT-aq) yielded 156.5 μmol $g_{catalyst}^{-1}.hr^{-1}$ of CH_4, which is in the top tier of reported performance values achieved using TiO_2 as a stand-alone photocatalyst. This performance resulted because appreciable amounts of CH_4 were generated under visible light illumination as well. TiO_2 nanotubes exhibited CO_2 photoreduction activity up to a wavelength of 620 nm with visible light driven photocatalytic activity peaking at 450 nm for flame annealed TiO_2 nanotubes. Isotope labelling studies, using GC–MS and gas-phase FTIR, indicated photoreduction of $^{13}CO_2$ to $^{13}CH_4$. The detection of ^{13}CO in the product mixture, and the absence of HCHO and HCOOH provides strong support for the photoreduction proceeding along a carbene pathway. The enhanced CO_2 photoreduction performance of FANT-aq is attributed to increased visible light absorption, square morphology, and the presence of rutile as the only crystalline phase with (110) as the dominant plane.

1. Introduction

The alarming rise of CO_2 concentrations in the atmosphere due to ever-increasing reliance of mankind on fossil fuels has intensified research to develop clean and carbon-neutral energy systems [1]. Numerous approaches such as CO_2 capture and storage [2], conversion of CO_2 into valuable products (*e.g.* cyclic carbonates and polycarbonate-polyols) [3], and microbial binding of CO_2 [4] have been proposed for fixation of CO_2 in extended time scales. The geological storage of CO_2 is an energy intensive approach, which is less promising due to the inherent risk of sudden leakages, huge energy requirements and acidification of sea water. The photocatalytic conversion of CO_2 into light hydrocarbons using sunlight as a source of energy and water as a source of electrons and protons is an enticing approach to control carbon emissions. Since the discovery of photoelectrochemical CO_2 reduction on GaP by Halmann in 1978 [5] and subsequent work on the photocatalytic reduction of CO_2 in aqueous suspensions of WO_3, TiO_2, CdS and ZnO [6], several semiconductor photocatalysts have been explored for CO_2 activation. However, none of these semiconductors meet the requirements for efficient and durable CO_2 reduction. Among various semiconductor materials TiO_2 has gained wide consideration due to its non-toxic nature, wide abundance, durability under extreme conditions, and appropriate band-edge positions for CO_2 reduction. The dominance of TiO_2 in the field of semiconductor-mediated artificial photosynthesis is such that H. Garcia and colleagues authored a review article in 2013 titled *Photocatalytic CO_2 Reduction using Non-Titanium Metal Oxides and Sulfides* and still found non-TiO_2 materials to be "notoriously inefficient" [7]. However, TiO_2 possesses a wide bandgap of 3.0–3.2 eV that restricts optical absorption to photons in the ultraviolet (UV) spectral range, where only a tiny fraction (~ 5%) of solar energy resides. Moreover, recombination losses are particularly pernicious for the reduction of CO_2 to fuels which involves 6–8 electron transfer steps [8].

Bandgap engineering using different schemes, *e.g.* doping with

* Corresponding authors at: Department of Electrical and Computer Engineering, University of Alberta, Edmonton, Alberta T6G 2V4, Canada.
E-mail addresses: pkar1@ualberta.ca (P. Kar), pawan@ualberta.ca (P. Kumar), kshankar@ualberta.ca (K. Shankar).

https://doi.org/10.1016/j.apcatb.2018.08.002
Received 20 May 2018; Received in revised form 23 July 2018; Accepted 1 August 2018
Available online 02 August 2018
0926-3373/

metals and non-metals, photosensitization with low band gap semiconductors as well as metal complexes, and composite formation with other semiconductors and carbonaceous materials, have been explored to improve visible light absorption in TiO_2. However, the yield of hydrocarbon reaction products has not exceeded a few micromoles per unit mass of catalyst. Flame annealed titania received significant attention in the early 2000s as a method to improve the visible light responsivity of TiO_2 through the introduction of defects and dopants [9–13]. In a highly cited but contentious study, S.U.M. Khan and colleagues reported on highly efficient water-splitting using flame annealed TiO_2 thin films in the journal *Science* in 2002 [9]. The results of these studies were challenged on the basis of spectral mismatch between the unfiltered Xe arc lamp used as the illumination source and the spectrum of terrestrial sunlight, potentially unphysical mechanisms used to explain the observed enhancement, and problems with the reproducibility of the reported results [14]. Consequently, this line of research was not widely pursued. Recently, there has been a resurgence of interest in "black TiO_2", which is a defect-rich form of reduced titania exhibiting visible light absorption over a broad spectral range, particularly for photoelectrochemical water-splitting [15–20].

The TiO_2 nanotube array structure affords the tremendous advantage of orthogonalization of the light absorption and charge separation processes [21–24]. The nature of anodic synthesis is such that the length of the nanotubes can be made as large as millimeters while the nanotube wall-thickness remains in the 5–30 nm range [25]. Thus, the nanotubes can be longer than the penetration depth of absorbed radiation while the wall-thickness of the nanotubes can be of the order of the carrier retrieval length (diffusion length + drift length due to surface band-bending [26–29]) such that a majority of the photogenerated carriers are able to reach the nanotube surface before recombination and/or trapping, and react with adsorbed reactants or electrolyte ions [30]. For this reason, one-dimensional TiO_2 nanostructures constitute some of the highest performing nanomaterial architectures for CO_2 reduction with reported CH_4 generation rates as high as 3.7 ml g^{-1} hr^{-1} [31,32]. Typically, the TiO_2 nanotubes are decorated with monometallic or bimetallic co-catalyst nanoparticles (NPs) containing at least one noble metal such as Pt, Pd, Rh, Ru, Au, Cu, CuPt, ZnPd, AuCu, *etc* [33–38]. The presence of the noble metal assists in electron-hole pair separation and reduced recombination through the introduction of surface band-bending, produces favorable shifts in the flatband potential of the photocatalyst for CO_2 reduction, introduces new adsorption modes for CO_2 adsorption, generates plasmonic enhancement (for Ag and Au containing systems), and promotes phonon-driven catalysis through a coupling of the vibrational modes of the metal to those of organic adsorbates. Yet, the presence of noble metals increases costs dramatically and reduces the possibilities of scale up and commercial deployment. Many metal co-catalysts are also vulnerable to poisoning by reaction products or intermediates [39,40].

In 2015, we reported on an unusual morphological transition from cylindrical nanotubes with circular or ellipsoidal cross-sections to jar-shaped nanotubes with square cross-sections that resulted from flame annealing of anodically formed TiO_2 nanotubes [23]. This morphological transition was accompanied by other unusual features such as the reduction in carrier density in the nanotubes by over an order of magnitude and a significant negative shift in the flat band voltage. In photoelectrochemical measurements in 1 M KOH, the flame annealed TiO_2 nanotubes (FANTs) outperformed low temperature annealed anatase-phase nanotubes (LANTs) and high temperature furnace-annealed dominant rutile-phase nanotubes (HANTs) by a factor of three to five [23]. Herein, we report on the CO_2 reduction performance of FANTs as a stand-alone photocatalyst without any noble metal co-catalysts.

Phase pure rutile and mixed phase (rutile and anatase) square shaped TiO_2 nanotube arrays are formed by flame annealing, and an enhanced photoreduction performance is demonstrated for the photoreduction of CO_2 to CH_4 in simulated solar light and visible light alone (without any ultraviolet component) conditions. Flame annealed TiO_2 nanotubes with square-shaped pore morphologies were synthesized by electrochemical anodization in ethylene glycol based electrolyte (FANT-eg) and water based electrolyte (FANT-aq) followed by elevated temperature (750 °C) flame annealing. The CO_2 photoreduction performance of flame annealed TiO_2 nanotubes was compared to low temperature annealed nanotubes as synthesized in ethylene glycol based electrolyte (LANT-eg) and water based electrolyte (LANT-aq). While our isotope labelling experiments using gas chromatography with a mass spectrometric detector (GC–MS) and gas-phase Fourier transform infrared spectroscopy (FTIR) confirmed photoreduction of CO_2 to CH_4, we also performed systematic control experiments to verify the same. The importance of this work originates from the demonstration of bare TiO_2 nanotubes (*i.e.* without functionalization, intentional doping, *etc*.) formed using a simple solution-processing method, as efficient catalysts for the photoreduction of CO_2 to CH_4.

2. Materials and methods

2.1. Materials

Ammonium fluoride (> 98%), aqueous hydrofluoric acid (49%), ethylene glycol, EG (> 99%) and acetic acid (> 99%) were obtained from Fisher Chemical and used in their as-received form without any further purification. De-ionized water was used throughout this study, and all other solvents were of HPLC grade. Titanium Foil (99%, 0.89 mm thickness) was procured from Alfa Aesar. Ti foil was cut into 1 cm x 2.5 cm pieces and washed by sonication in water, methanol and acetone each for 10 min to remove any organic/inorganic contaminant. $^{12}CO_2$ was of 99% purity and was obtained from Praxair (Canada). $^{13}CO_2$ of 99% purity was obtained from Cambridge Isotope Laboratories, Inc. (USA).

2.2. Synthesis of TiO_2 nanotube arrays

Ethylene glycol (EG)-based organic electrolyte and water-based electrolyte were the two different recipes used to anodically form two different types of TiO_2 nanotubes. The EG-based electrolyte contained 0.3 wt% NH_4F and 4% v/v of deionized water. The water-based electrolyte contained 4% v/v of HF and 8% v/v of acetic acid. The anodization process using water-based electrolyte was performed at room temperature in a two-electrode electrochemical cell using a graphite cathode at an applied voltage of 15 V. Anodization using EG-based electrolyte was also performed under identical conditions except that the applied voltage between the Ti anode and graphite cathode was maintained at 30 V. The obtained TiO_2 nanotube arrays using aqueous and EG based electrolyte were annealed in air at 450 °C for three hours and denoted as LANT-aq (low temperature annealed nanotubes prepared in aqueous medium) and LANT-eg (low temperature annealed nanotubes in ethylene glycol), respectively. Flame annealing was performed at high temperature (~ 750 °C) using a propane torch for about 2 min, and the resulting flame annealed nanotubes are called FANT-aq (flame annealed nanotubes prepared in water-based electrolyte) and FANT-eg (flame annealed nanotubes prepared in EG-based electrolyte).

2.3. Characterization

The nanoscale morphologies of the TiO_2 nanotubes were imaged using a field emission scanning electron microscope (FESEM, Hitachi-NB5000). X-ray diffraction (XRD) was performed using a glancing angle configuration in a Bruker D8 Discover instrument with a sealed Cu Kα X-ray source (40 kV, λ = 0.15418 nm). Raman spectroscopic data was collected using a Nicolet Almega XR Raman Spectrometer with an incident laser wavelength of 532 nm and at an incident power of 24 mW. High-resolution transmission electron microscopy (HR-TEM) imaging to investigate fine morphological features was performed using a JEOL

2200 FS TEM at an acceleration voltage of 200 kV. Optical characterization was performed using a Perkin Elmer Lambda-1050 UV–vis-NIR spectrophotometer equipped with an integrating sphere accessory. X-ray photoelectron spectra (XPS) for determining oxidation state and surface chemical composition of materials was acquired using an Axis-Ultra (Kratos Analytical) instrument equipped with monochromatic Al-Kα source (15 kV, 50 W) and photon energy of 1486.7 eV under ultra-high vacuum ($\sim 10^{-8}$ Torr). The binding energy of C1 s core level (BE ≈ 284.8 eV) of adventitious hydrocarbon was used as a standard to assign the binding energies of other elements. The raw data was deconvolved into various peak components using CasaXPS and later plotted in Origin 8.5. Brunauer–Emmett–Teller (BET) specific surface area measurement of the nanotubes, after being scraped off from the Ti foil, was performed using an Autosorb iQ device. For BET measurement, nitrogen gas was used, degassing was performed at 350 °C and surface area was measured at −193 °C. To determine the presence of Ti^{3+} and O^{2-} species, X-band continuous wave electron paramagnetic resonance (EPR) spectra of materials were recorded using a Bruker model E-580 (EMXnano) spectrometer (Germany) equipped with an Oxford CF935 helium flow cryostat. For the measurement, sample was scratched from Ti foil, charged in quartz tubes covered with air tight lids and EPR spectra were collected at 100 K using liquid nitrogen. Time-resolved photoluminescence (PL) data, was obtained using 2-photon fluorescence lifetime imaging microscopy (FLIM). The excitation was by a femtosecond Ti:sapphire laser at a wavelength of 750 nm. Imaging was performed using a Zeiss LSM 510 NLO multi-photon microscope equipped with a FLIM module, which comprised a Hamamatsu RS-39 multichannel plate detector, a filter wheel, and a Becker Hickl Q5 SPC730 photon-counting board.

2.4. Photocatalytic CO_2 reduction experiments

CO_2 photoreduction experiments were performed in a cylindrical reactor with a transparent quartz window, and an internal volume of 32 mL as described in our earlier reports [32,36,41]. Single pieces of TiO_2 nanotube array photocatalyst with an active area of 1 cm x 2 cm were placed inside the reactor, and a few droplets of water were placed in the reactor beside the catalyst without direct contact with the catalyst. Then the reactor was closed, and purged with CO_2 to remove any other gases using a two valve system, followed by pressurizing the reactor (housing the photocatalyst and water droplets) with 50 psi of CO_2. The photoreactor was heated to ~ 80 °C using a hot plate to convert the water droplets in the reactor into water vapor, and the photocatalyst was irradiated using the collimated AM 1.5 G output of a Newport Class A solar simulator having an intensity of 100 mW cm^{-2} on the photocatalyst surface at a distance of 32 cm from the light source. In order to investigate visible light induced photocatalysis, experiments were also performed wherein the catalysts were respectively illuminated using a 50 W LED lamp (maximum intensity around 510 nm) with filtered out UV light, and the same with a 650 nm high pass filter. In order to understand the wavelength dependence of photocatalytic activity, monochromatic LEDs of different wavelengths (400 nm, 450 nm, 500 nm and 620 nm), each with an output power intensity of 10 mW cm^{-2} were used for irradiating the samples. After 2 h of irradiation the reactor gas samples were analyzed using gas chromatography (GC model: SRI 8610C Gas Chromatograph) by injecting samples into the sample loop (1 mL) of the GC using simple Swagelok piping. The GC was equipped with a 10′ HayeSep D 1/8″ packed column, a thermal-conductivity detector (TCD), and a flame ionization detector (FID). Gases were eluted from the column isothermally at 85 °C for 10 min. Helium was used as the carrier gas and its flow rate through the column was maintained at 25 mL min^{-1}. Isotopic labelling experiments were performed using $^{13}CO_2$ to verify the origination of methane from photocatalytic reduction of CO_2. The obtained reaction product containing $^{13}CH_4$ was analyzed with gas chromatography-mass spectrometry (GC–MS) using an Agilent 7890 A GC/MS instrument. Gas phase FTIR analysis (for detection of $^{13}CH_4$) was performed using a Magna System 750 FTIR, equipped with an IR source and detector (MCT/B). The FTIR system had a 4.8 m multiple bounce gas cell (Infrared Analysis Inc. Anaheim USA, Model G-2-4.8-PA-BA-AG), and was evacuated to 100 mTorr and backfilled with dry argon (UHP 5.0 Praxair). This procedure was repeated three times, then the gas cell was evacuated to 100 mTorr and a background acquired. The background spectrum was saved and used for subsequent data collection. Gas from the photoreactor was sampled directly from the reactor outlet port into a 0.25 L Tedlar bag. The sample was introduced directly into the gas cell by connecting the Tedlar bag valve to the gas cell valve. The sample spectrum was acquired with 400 Torr gas pressure inside the gas cell.

2.5. Optical simulations of nanotube arrays

Optical properties of the LANT and FANT-eg structures were investigated using Lumerical FDTD simulation software. LANT structures were simulated as nanotubes with circular cross-sections with inner and outer radii of 40 and 70 nm respectively, and height of 300 nm. Similarly, FANT-eg structures were simulated as nanotubes also of height 300 nm but with square cross-sections. The simulations were performed for both combinations of individual nanotubes in vacuum. Near-field, and far-field profile and frequency monitors were utilized to capture scattering and absorption cross sections, electric field intensity profiles, Poynting vector distributions as well as reflection and transmission spectra. Material-specific optical properties of anatase in LANT-eg, and mixed rutile (42%) - anatase (58%) in FANT-eg structures were simulated using the appropriate refractive index data, as obtained *via* ellipsometry. Refractive index data corresponding to the anatase TiO_2 were obtained from Siefke et al. [42] The effective medium approximation for the mixed-phase materials was determined *via* Bruggeman's model, labelled as Eq. (1)

$$\sum_i \delta_i \frac{\sigma_i - \sigma_e}{\sigma_i + (n-1)\sigma_e} = 0 \quad (1)$$

where δ_i and σ_i are respectively the fraction and refractive index of each component, and σ_e is the effective conductivity of the medium. Lumerical's refractive index monitor was utilized to confirm the structures were appropriately configured and identified by the software throughout the course of the simulation. The structures were illuminated by a light source incident at a normal angle from above with a bandwidth range of 350 − 800 nm. Snapshots of the electric field intensity profiles, and Poynting vector distributions were taken at specific wavelengths between 350 − 500 nm in 50 nm increments, and as viewed along different planes including the *xy*-, *xz*-, and *yz*-planes. The symmetry of the structures were considered by setting appropriate symmetric and anti-symmetric boundaries allowing for shorter simulation times, and accurate data aggregation.

3. Results and discussion

3.1. Morphology, structure and chemical composition of regular- and flame annealed nanotubes

Fig. 1 is a schematic illustration of the flame annealing process. High-temperature annealing stimulates phase transformation from anatase to rutile which proceeds *via* a square-shape morphological change (SEM image in inset of Fig. 1).

The cross-section and top-view FESEM images of the TiO_2 nanotubes are shown in Fig. 2, from where their dimensions and distinguishing morphologies are evident. The average length of FANT-eg was found to be ~ 2 μm, while the same for FANT-aq was found to be 200 nm. The length of the nanotubes does not change significantly after flame annealing for both types of nanotubes. However, the pores of FANT-eg nanotubes are transformed from circular to square shaped. The average inner width of square pores of FANT-eg is 50 nm, while the

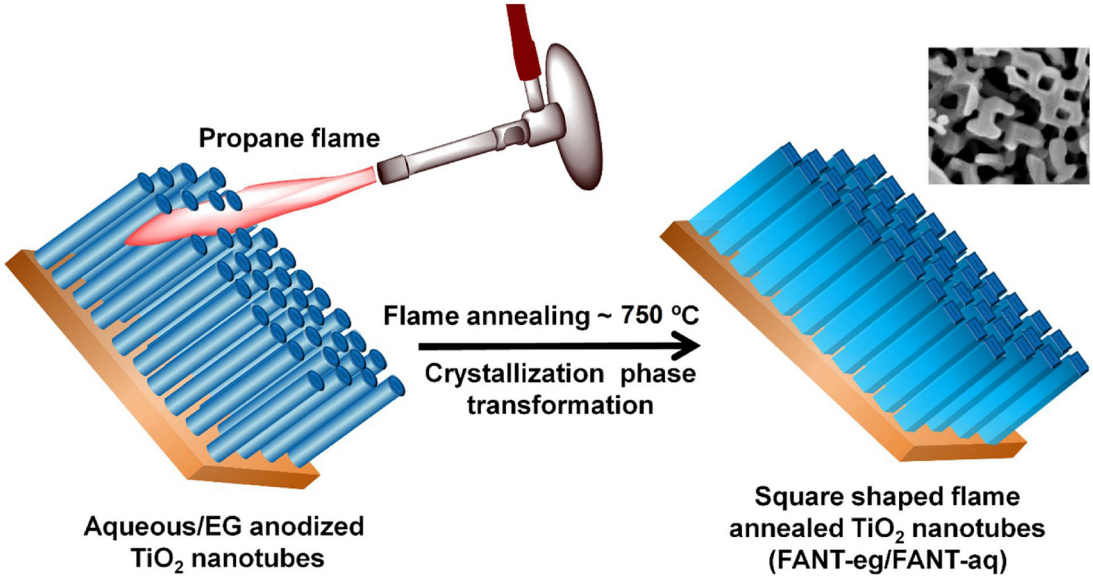

Fig. 1. Schematic of synthesis of square shaped flame annealed TiO_2 nanotubes.

same for FANT-aq is 80 nm. The average wall thickness values for FANT-eg and FANT-aq are 40 nm and 20 nm respectively. The average pore diameter is 80 nm for both LANT-eg and LANT-aq while the average wall thickness values for LANT-eg and LANT-aq are 20 nm and 15 nm respectively. To estimate the mass of the nanotubes, the fill fraction (f_{s1}) of TiO_2 was determined as a fraction of the free space the nanotubes occupy.

The fill fractions for LANT-eg and LANT-aq were calculated using Eq. (2) [43–45] and the fill fractions for FANT-eg and FANT-aq was calculated using Eq. (3)

$$f_{s1} = \frac{\frac{2t}{R_0} - \left(\frac{t}{R_0}\right)^2}{\frac{2\sqrt{3}}{\pi}\left[\left(\frac{s}{2R_0}\right)^2\right]} \quad (2)$$

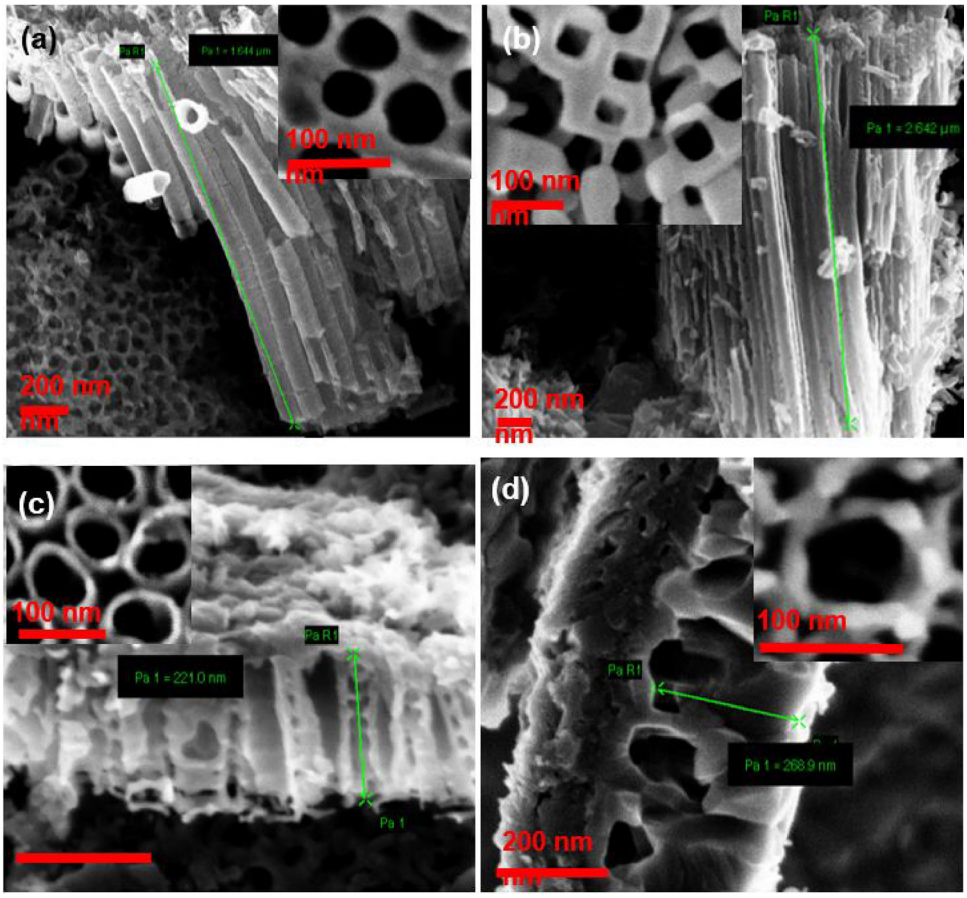

Fig. 2. Cross-section FESEM images of LANT-eg (a), FANT-eg (b), LANT-aq (c) and FANT-aq (d). Insets are top-view FESEM images of the same.

Table 1
Measured dimensions, fill fraction, and mass per unit area of TiO_2 nanotubes used in this study.

Nanotube type	Average nanotube length (μm)	Average nanotube pore diameter (nm)	Average nanotube wall thickness (nm)	Nanotube fill fraction	Nanotube mass per unit area (g cm^{-2})
FANT-aq	0.2	80	20	0.106	8.97×10^{-6}
LANT-aq	0.2	80	15	0.104	8.09×10^{-6}
FANT-eg	2	50	40	0.497	4.01×10^{-4}
LANT-eg	2	80	20	0.367	2.86×10^{-4}

$$f_{sl} = \frac{T_o^2 - T_i^2}{T_o^2} \quad (3)$$

In Eq. (2), t is the average wall thickness and R_0 is the average radius of nanotubes, and s is the distance between adjacent nanotubes. In Eq. (3), T_o and T_i are the widths of the outer and inner edges of the square-section of the nanotubes. Using the relevant dimensions of the nanotubes, fill fractions calculated using Eqs. (2) and (3), and are displayed in Table 1. Using these fill fraction values, the mass of the nanotubes per unit area was also calculated, and is also shown in Table 1. While mass of the nanotubes were reliably calculated, our measured specific area of the EG anodized TiO_2 nanotubes was 583 $m^2 g^{-1}$, which is consistent with values reported in literature [46,47]. Due to requirement of a large quantity of TiO_2 nanotube powder, we only performed BET surface area analysis on the longer EG anodized TiO_2 nanotubes. The specific areas of LANT-eg and FANT-eg were similar.

The fine structural features of the nanotube photocatalysts were determined with HR-TEM (Fig. 3). High temperature annealing promoted the formation of the thermodynamically stable rutile phase of TiO_2. Images of FANT-eg at 5 nm scale bar (Fig. 3a) show various domains of lattice fringes, having 0.33 nm and 0.21 nm inter-planar d-spacings associated with the rutile (110) and anatase (004) planes of TiO_2. The appearance of these planes reveals the presence of both anatase and rutile phase TiO_2 domains in FANT-eg (Fig. 3a). The TEM image of TiO_2 nanotubes prepared using the aqueous recipe after flame annealing (FANT-aq) exhibits rutile phase alone; the 0.27 nm and 0.18 nm d-spacings in Fig. 3b respectively correspond to the (101) and (211) planes of rutile TiO_2. These phase transformations together with thermal stresses during flame annealing are likely responsible for the change in cross-section of TiO_2 nanotubes from circles to square shapes [23,48]. LANT-eg and LANT-aq samples, annealed at 450 °C, show only the (101) and (004) planes of anatase phase TiO_2 with 0.35 nm and 0.25 nm d-spacing respectively (Fig. 3e and f). The presence of sharp diffraction rings in the selected area diffraction pattern of FANT-eg shows polycrystalline nature (Fig. 3c). Diffraction rings corresponding to (101), (004), (200), (220) planes of anatase and (110), (211), (220), (002), (310) planes of rutile were observed in the SAED pattern of FANT-eg in Fig. 3c, which further confirmed the presence of both anatase and rutile phases of TiO_2 in the nanotubes. The SAED pattern of FANT-aq showed diffraction rings related to rutile phase TiO_2 alone (Fig. 3d). LANT-eg and FANT-aq displayed only anatase phase diffraction rings (Fig. 3g and h). The obtained results were fully consistent with XRD and Raman findings shown in Figs. 4 and 5 respectively.

A question that arises is what reason exists for the FANT-aq samples to be completely transformed from anatase into rutile by flame annealing while the FANT-eg samples are composed of a mixture of 52% anatase and 48% rutile. To answer this question, we must understand two aspects – one related to nanotube length and the other related to the anodization electrolyte. A higher annealing temperature promotes the anatase-to-rutile phase transition. The nanotubes grown in aqueous electrolyte (LANT-aq) are relatively short (0.2 μm nanotube length as indicated in Table 1) and the flame annealing process, which directly provides heat to the top surface of the nanotubes, is easily able to generate similarly high temperatures at the bottom of the nanotubes as it does at the top surface (small temperature gradient). On the other hand, the nanotubes grown in EG electrolyte are 2 μm long (Table 1) and there is a much higher chance of a temperature gradient persisting that would prevent the bottom parts of the nanotubes from reaching the temperatures generated by flame annealing at the top surface. Secondly, it is well known that nanotubes formed by anodization in EG-based electrolytes possess a higher amount of embedded fluoride ions [49]. Further, it is well-established that the incorporation of fluoride ions retards the anatase-to-rutile phase transformation due to which the FANT-eg samples retain a significant anatase fraction [49].

For further confirmation of these phases, we analyzed the samples using XRD. For FANT-aq, the XRD pattern (red curve in Fig. 4) showed phase pure rutile, indicated by a dominant (110) peak at 27.4° (JCPDS No. 21-1276) while FANT-eg (blue curve in Fig. 4) showed the rutile (110) peak at 27.4° (JCPDS No. 21-1276) in addition to anatase (101) peak at 25.2° (JCPDS No. 21-1272), which demonstrates the presence of both anatase and rutile phase TiO_2. The same XRD curve of FANT-eg is shown again in Fig. 4b, to highlight the presence of both anatase and rutile phases. The percentage of rutile phase in the anatase and rutile mixture in FANT-eg was calculated using Eq. (4) [50] by measuring intensities of the most intense anatase (101) and rutile (110) peaks, and was found to be 42.72%.

$$R = \frac{I_R}{I_R + 0.884 I_A} \quad (4)$$

In Eq. (4), R is the rutile percentage while I_R and I_A are the intensities of rutile and anatase peaks respectively. The optimum rutile percentage for obtaining the best photocatalytic performance has been previously reported to be between 20 and 40% [[51] [52],]. Therefore, XRD data suggests close to optimum rutile phase content in FANT-eg samples. XRD patterns of LANT-eg (green curve in Fig. 4) and LANT-aq (blue curve in Fig. 4) exhibit regular anatase peaks, which conform to the relatively low temperature annealing condition (*i.e.* 450 °C) that promotes the formation of phase pure anatase. Grain sizes of the nanotubes varied with annealing temperature as well, and were calculated using the Scherrer equation, shown as Eq. (5) below:

$$S = \frac{K\lambda}{\beta \cos\theta} \quad (5)$$

In Eq. (5), S is the mean size of crystalline domains, K is a dimensionless shape factor (assumed as 1), λ is the X-ray wavelength which is 0.154 nm (Cu Kα source), β is the peak width at half of the maximum intensity in radians, and θ is the Bragg angle. β was obtained using Lorentzian fits of the anatase (101) and rutile (110) peaks, as shown in Figs. S2 (a, b, c and d). The obtained crystallite grain sizes are listed in Table 2. FANT-eg nanotubes show the largest crystallite size for both anatase (36.17 nm) and rutile phase (41.66 nm).

The Raman spectra (Fig. 5a) of FANT-eg and LANT-eg are characterized by peaks at 141 cm^{-1} [43], with a higher peak intensity in FANT-eg due to contributions from both the anatase Eg and rutile B1g Raman active modes [53,54]. Other Raman active modes of lower intensity are assigned to anatase. The Raman spectrum (Fig. 5b) of FANT-aq is characterized by an intense peak at 141.1 cm^{-1}, which we attribute to rutile B1g by correlating with XRD and TEM data for the nanotubes. A similar peak, although slightly blue-shifted, appears in the Raman spectrum (Fig. 5b) of LANT-aq, which we attribute to the anatase Eg mode. Distinct Raman active modes, corresponding to rutile Eg and A1g, as well as a band corresponding to a multi-phonon processes,

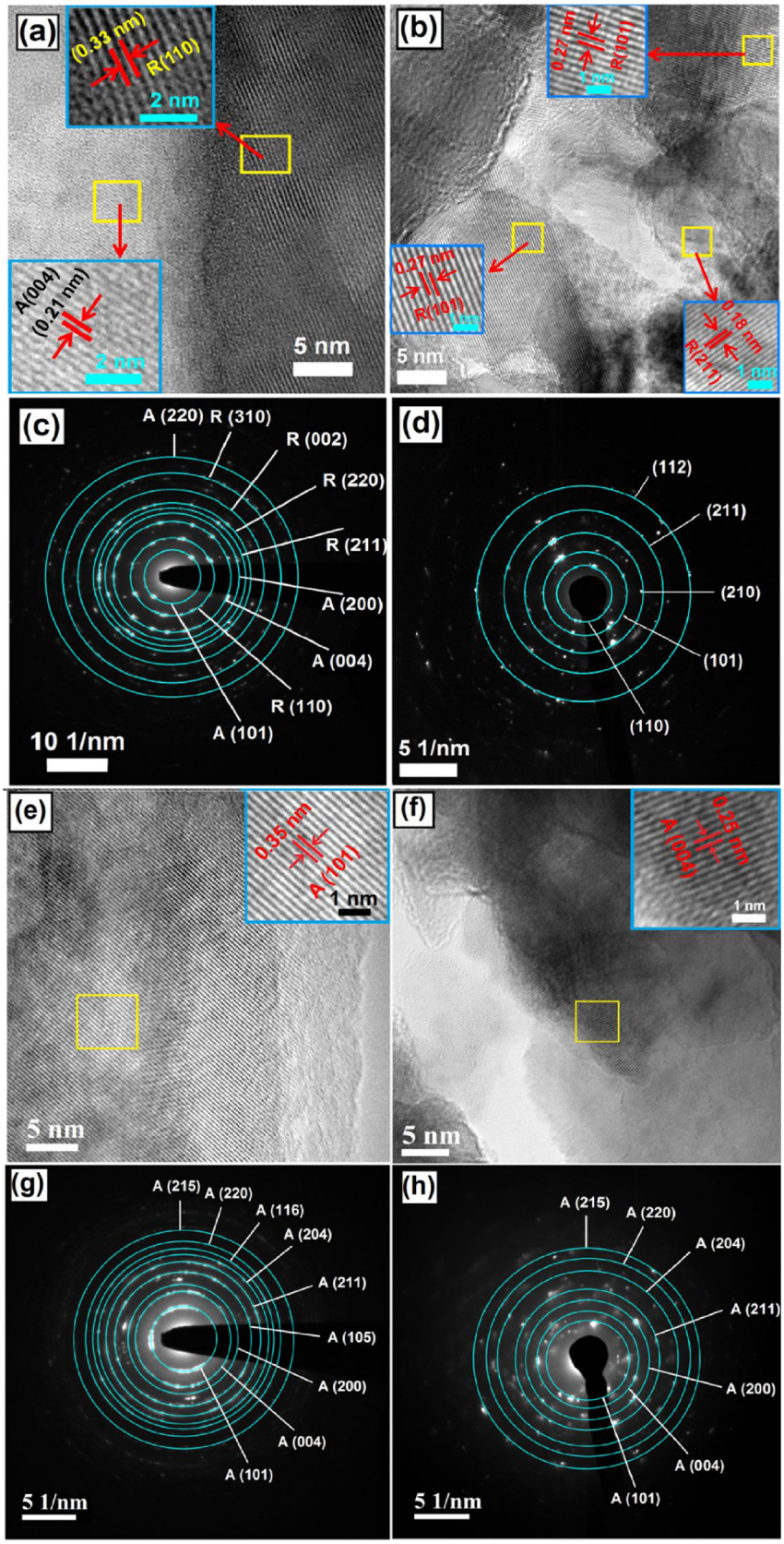

Fig. 3. HR-TEM images showing fringe patterns and 2d spacing of FANT-eg (a), FANT-aq (b), LANT-eg (e) and LANT-aq (f); SAED patterns of FANT-eg (c), FANT-aq (d), LANT-eg and (g) LANT-aq (h).

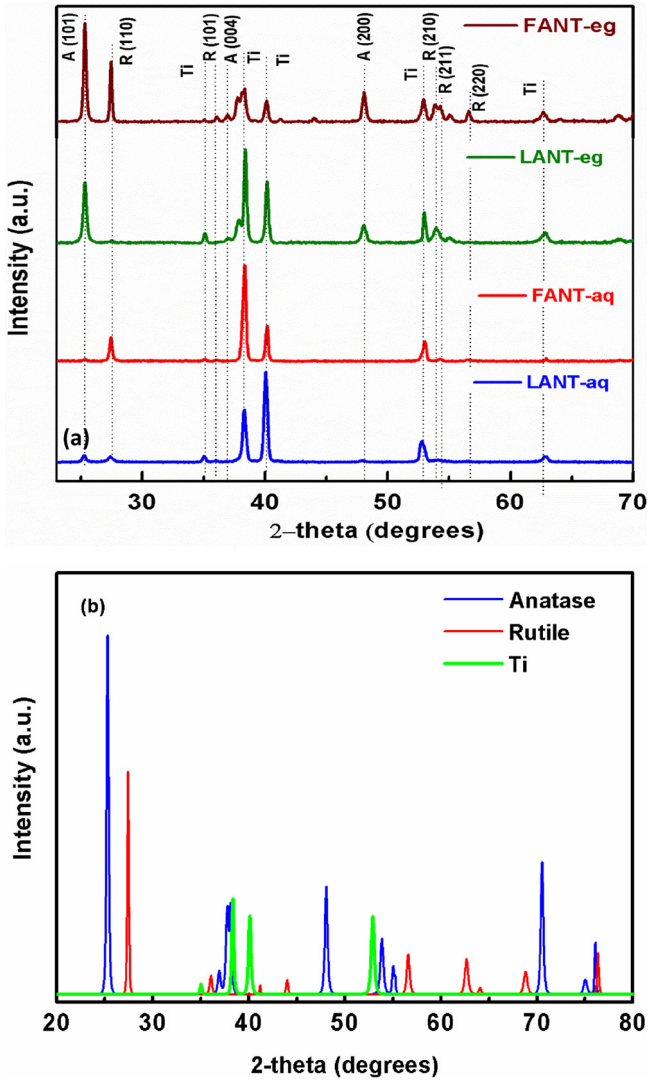

Fig. 4. (a) Glancing angle XRD patterns of FANT-eg, LANT-eg, FANT-aq, and LANT-aq (b) Glancing angle XRD pattern of FANT-eg specifically, highlighting the mixed phase nature by separating the signal from each phase.

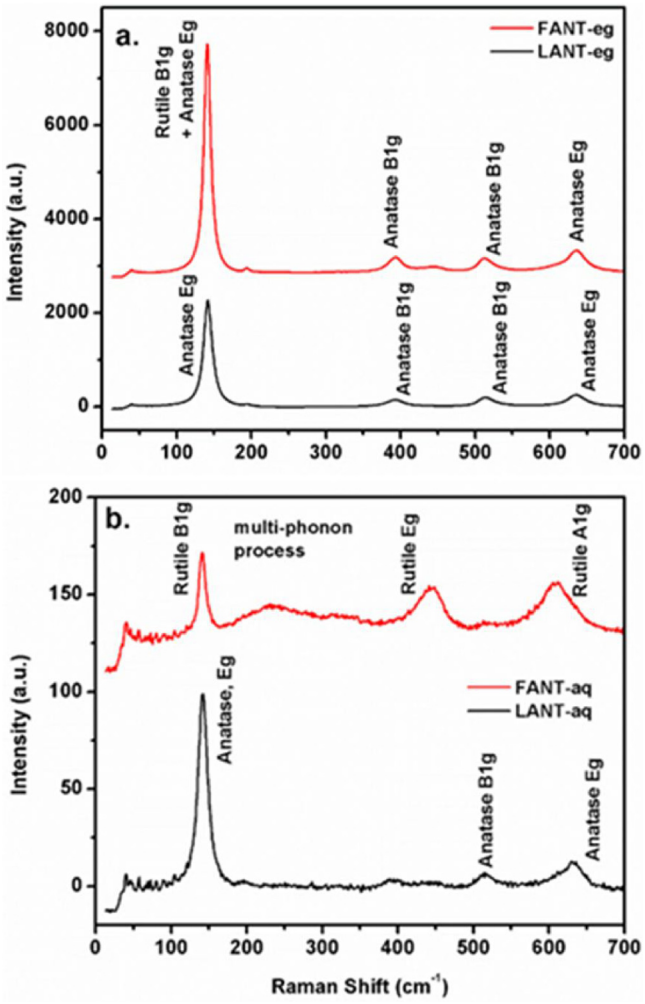

Fig. 5. Raman spectra of: (a) FANT-eg, and LANT-eg; and (b) FANT-aq, and LANT-aq.

are also observed in the Raman spectra of FANT-aq [55]. Lower intensity anatase peaks B1g and Eg, appear in the Raman spectra of LANT-aq. Phonon lifetimes (τ) were calculated using the time-energy uncertainty relation (Eq. 6) [56] for the Eg mode in the Raman spectra of the nanotubes.

$$\frac{1}{\tau} = \frac{\Delta E}{\hbar} \tag{6}$$

In Eq. (6), ΔE is the FWHM, which was obtained from Lorentz fits of Eg peaks of the nanotubes, as shown in Fig. S3 (a, b, c and d); $\hbar = 5.3 \times 10^{-12}\,\mathrm{cm}^{-1}$.s, and τ is the phonon lifetime. Values of phonon lifetimes of the nanotubes are listed in Table 2.

The optical properties of regular and flame annealed nanotubes were examined with diffuse reflectance UV–vis spectroscopy (Fig. 6). The UV–vis absorption spectrum of LANT-aq (black curve in Fig. 6) showed a sharp band edge at 386 nm characteristic of the anatase bandgap (3.2 eV) which was redshifted to 410 nm in FANT-aq (red curve in Fig. 6). This is characteristic of the bandgap of rutile (3.0 eV), and occurs due to the anatase to rutile phase transition previously explained. On the other hand, the band-edge for both LANT-eg and FANT-eg samples is at *ca.* 400 nm. Additionally, a broad hump around 450 nm was also observed for LANT-aq which is known to originate from defects and midgap trap states in anatase TiO_2 [57–59]. Another broad absorption band extending from 550 to 750 nm is likely due to metallic d-orbital transition of the Ti foil substrate [60]. Both the FANT-eg and FANT-aq samples exhibited a monotonically increasing longer wavelength absorption which is attributed to the Drude absorption of conduction band electrons in TiO_2 [61]. The non-monotonic extended visible absorption of FANT-eg (cyan curve in Fig. 6) and LANT-eg (blue curve in Fig. 6) are due to the localized excitation of Ti^{3+} states vis $3d \rightarrow 3d$ transitions [62]. The Ti^{3+} states are created due to relatively more reducing conditions during anodic synthesis in organic electrolytes [63] which are not completely oxidized even after thermal annealing. FANT-aq showed a band tail around 410 nm. PL lifetime decay data (Fig. S3) for FANT-eg and LANT-eg were fitted to single exponential decay curves while the data for FANT-aq was fitted to bi-exponential decay curve, and the data for LANT-aq was fitted to a single exponential decay. FLIM data indicated an increase in PL lifetime because of flame annealing of the nanotubes. 2-photon fluorescence images are shown in Fig. S4, where it can be observed that the flame annealed nanotubes (FANT-eg and FANT-aq) are more fluorescent than the non-flame annealed nanotubes (LANT-eg and LANT-aq). The higher fluorescence intensity and longer lifetimes are due to suppressed non-radiative recombination processes [64,65].

The surface chemical composition and presence of defects were validated using X-ray photoelectron microscopy. Elemental survey scans (Fig. S5) of all nanotubes samples exhibit peaks corresponding to Ti2*p* and O1*s* (Fig. 7). High resolution XPS spectra of all TiO_2 nanotubes in Ti2*p* region can be de-convolved into four peak components. The

Table 2
Crystallite grain sizes of nanotubes, phase percentage, positions and widths of the Raman Eg modes, phonon lifetimes of the nanotubes, and Ti^{4+}/Ti^{3+} ratio.

Nanotube type	Crystallite size, anatase (101) (nm)	Crystallite size, rutile (110) (nm)	Crystalline Phase	Raman Peak position (cm^{-1})	Raman FWHM (cm^{-1})	Phonon lifetime (ps)	Ti^{4+}/Ti^{3+}
FANT-aq	–	36.18	100 % Rutile	141.23	11.09	0.48	12.67
LANT-aq	31.45	–	100 % Anatase	141.14	11.24	0.47	9.72
FANT-eg	36.17	41.66	100 % Anatase	141.11	11.24	0.47	8.91
LANT-eg	29.36	–	42 % Rutile 58 % Anatase	141.85	14.36	0.37	9.46

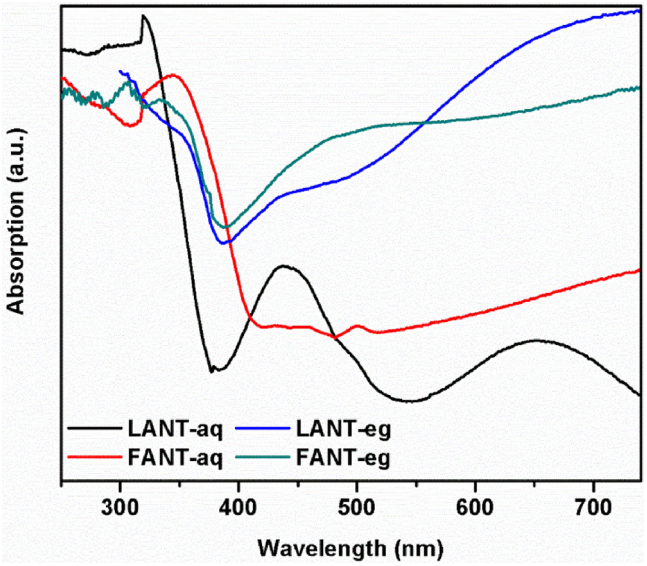

Fig. 6. UV–vis spectra of the nanotubes.

major peak components at binding energies of 458.6 eV and 464.4 eV were assigned to $Ti2p_{3/2}$ and $Ti2p_{1/2}$ core level transitions of Ti^{4+} [35,66,67]. Two minor peaks at lower binding energies, 457.88 and 463.3 eV, were attributed to $Ti2p_{3/2}$ and $Ti2p_{1/2}$ peak components of Ti^{3+} present in the form of lattice defects [68–70]. As anticipated, for FANT-eg nanotubes the ratio of Ti^{4+} to Ti^{3+} was found to be lowest (8.91, shown in Table 2) which suggests that flame annealing and phase transformation at higher temperatures facilitate the abstraction of some lattice oxygen that created oxygen vacancies and Ti^{3+} states. The presence of Ti^{3+} and oxygen defects creates defect levels below the conduction band which facilitate sub-bandgap electronic transitions [71–73]. The de-convolved HR-XPS spectra of all nanotubes in O1*s* display two peak components at binding energyies of 528.8 and 531.6 eV (Fig. 7). The strong peak at 528.8 eV originated due to oxygen atoms bonded to Ti atoms (Ti-O-Ti) in TiO_2 lattice while the peak shoulder component at *ca.* 531.6 eV appeared due to the presence of non-lattice adventitious oxygen and surface −OH groups [74]. The peak intensity of the non-lattice bonded oxygen peak component was substantially larger for TiO_2 nanotubes prepared in aqueous medium in comparison to TiO_2 nanotubes prepared in EG solvent which indicate that even after annealing some residual oxygen was present on the surface of aqueous nanotubes.

Since XPS provides only surface chemical information limited to 10 nm and ejected photoelectrons may contribute to Ti^{3+} XPS signal due to reduction of Ti^{4+} species *via* high energy photoelectrons. Further, Ti^{3+} states are vulnerable to oxidation under O_2 and can only be sustained for a short time. Hence, to validate the presence of Ti^{3+} species and surface defects in bulk material, X-band EPR spectra of highly performing flame annealed EG based nanotubes (FANT-eg) was collected at 100 K under dark conditions. The low temperature EPR spectra of FANT-eg exhibits an intense Lorentzian signal at *g* value of 2.001. The EPR signal at $g \approx 2.001$ corresponded to O_2^- was observed due to reduction of surface adsorbed O_2 *via* surface Ti^{3+} species, and indicates presence of plenty of Ti^{3+} species in the sample [67,75–77]. In addition, a weak broad signal at *g* value of 1.973 confirms existence of Ti^{3+} species in the samples which originated due to oxygen-centered surface hole trapping sites during the flame annealing process. The Ti^{3+} peak was broad which suggests distribution of coordination environment of surface centered radicals [17,76,78]. We have included this information in Figure S6 in ESI.[1] The EPR signal at $g = 4.266$ is said to derive from dopant species *i.e.* Fe^{3+}, V^{4+}, *etc* but might also originate from Ti self doping [79,80].

3.2. CO_2 photoreduction performance of regular and flame annealed TiO_2 nanotubes

The performance of the four types of titania nanotube samples was investigated for heterogeneous photocatalysis. Vapor phase CO_2 photoreduction experiments were performed using the solid phase TiO_2 nanotubes as the photocatalyst in the presence of CO_2 and water vapor as reactants under exposure to light from different sources for two hours. The photocatalytic CH_4 production per hour of reaction time, per unit mass (μmol $g_{catalyst}^{-1}$ hr^{-1}) of catalyst is shown in Table 3. Fig. S7 in the supporting information shows the photoreduction performance for specific narrow spectral bands of FANT-eg and LANT-eg samples at an illumination intensity of 10 mW cm^{-2}. It is evident from Table 3 that under simulated solar light condition, flame annealed nanotubes exhibited extremely high CH_4 production rate (156 μmol $g_{catalyst.}^{-1}$ $hr.^{-1}$ for FANT-aq and 9.5 μmol $g_{catalyst.}^{-1}$ hr^{-1} for FANT-eg). Under identical conditions the yields of CH_4 from CO_2 photoreduction were found to be 92 μmol $g_{catalyst}^{-1}$ hr^{-1} and 2 μmol $g_{catalyst}^{-1}$ hr^{-1} for LANT-aq and LANT-eg, respectively. Under illumination with a 50 W LED lamp light (maximum intensity at $\lambda_{max} = 510$ nm) with a filtered out UV component, CH_4 yield with the flame annealed TiO_2 nanotubes dropped significantly for FANT-aq (68 μmol $g_{catalyst}^{-1}$ hr^{-1}) while it remained almost the same for FANT-eg (9 μmol $g_{catalyst}^{-1}$ hr^{-1}). The decrease in CH_4 yield for FANT-aq during illumination using the broadband visible LED lamp is in agreement with the UV–vis spectrum of FANT-aq, which exhibited an absorption edge at 410 nm. Upon illumination with LED lamp light (with filtered out UV light) with a 650 nm long pass filter, the yield of CH_4 further decreased for all nanotube samples, as expected. Markedly higher photocatalytic CH_4 yields were observed with flame annealed TiO_2 nanotubes (FANT-eg and FANT-aq) than those with furnace annealed TiO_2 nanotubes (LANT-eg and LANT-aq). The observed CH_4 yields with the flame annealed TiO_2 nanotubes in this work exceed most reports with stand-alone TiO_2 catalysts, and are either comparable to or exceed CH_4 yields obtained with TiO_2-based functionalized catalysts and nanocomposites [36,81–90].

As mentioned earlier in this report, mass of the nanotubes is calculated by considering the nanotubes under a given irradiated geometrical area (or projected area to incident light), the fill fraction of nanotubes and length of the nanotubes. Therefore, in addition to measuring CH_4 yield in μmol $g_{catalyst}^{-1}$ hr^{-1}, the yield can be measured in μmol $cm^{-2}_{illuminated\ area}$, where the projected area is considered. The

[1] Electronic supplementary information available.

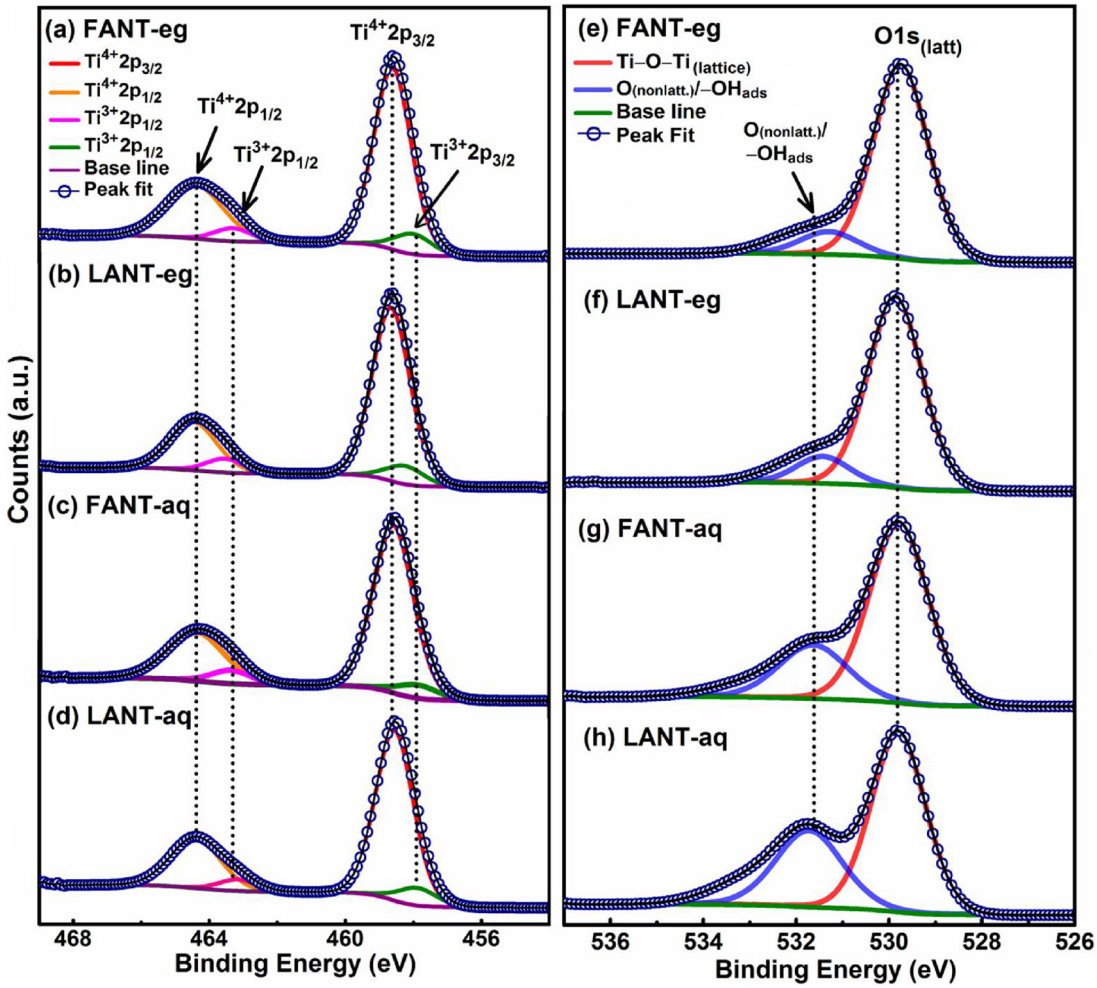

Fig. 7. High resolution XPS spectra of FANT-eg, LANT-eg, FANT-aq and LANT-aq in (a–d) Ti 2*p* region and (e–h) in O 1*s* region respectively.

Table 3
CH_4 yield by CO_2 photoreduction using FANT-eg, LANT-eg, FANT-aq, and LANT-aq, as well as some comparisons to previous literature.

Sample	Illumination Condition	CH_4 yield per unit mass (μmol. $g^{-1}.hr^{-1}$)	Reference
FANT-aq	AM 1.5 G, 100 mW cm^{-2}	156.5	–
	50 W LED lamp*	67.9	–
LANT-aq	AM 1.5 G, 100 mW cm^{-2}	92.0	–
	50 W LED lamp*	43.2	–
FANT-eg	AM 1.5 G, 100 mW cm^{-2}	9.5	–
	50 W LED lamp*	8.8	–
LANT-eg	AM 1.5 G, 100 mW cm^{-2}	2.0	–
	50 W LED lamp*	1.1	–
TiO_2 Microspheres with 0.6 wt.% Pt Loading	Hg UV Lamp	2.0	[81]
Pd-TiO_2 Particles	Light > 310 nm wavelength	0.4	[83]
CuO-TiO_2 Hollow Spheres	Hg UV Lamp	2.0	[84]
TiO_2 Nanoparticles	UV Light	0.6	[85]
Carbon Nanotube-Supported TiO_2	15 W 365 nm UV Lamp	14.7	[95]
Graphene Supported TiO_2	300 W Xe arc Lamp	27.4	[88]
TiO_2 Nanoparticles	8 W Hg Lamp	9.5	[96]

*50 W LED lamp with maximum intensity at 510 nm, and with an inbuilt UV filter.

projected surface area of a photocatalyst determines the amount of non-concentrated solar energy that it is incident on it for potential transformation into chemical energy. CH_4 yields (Fig. S8) obtained using FANT-aq, LANT-aq, FANT-eg, and LANT-eg, were found to be 0.0014, 0.0007, 0.00383, and 0.0006 μmol cm^{-2} $_{illuminated.area}$, respectively, under illumination by simulated sunlight (AM 1.5 G one sun, 100 mW cm^{-2}). Although our reported CH_4 yield appeared in nM cm^{-2}, there are literature reports [91], which mention CH_4 yield per unit area, wherein the yields are similar or smaller than that reported by us. Upon initial inspection, it would seem that FANT-eg samples are now outperforming FANT-aq under this different metric; the reason for this disparity is due to the length of the nanotubes used (reported in Table 1). Generally, longer EG anodized nanotubes (LANT-eg and FANT-eg) absorb a larger fraction of incident light than aqueous nanotubes, and as a result, produce larger amounts of CH_4 per unit illumination area than the shorter nanotubes formed in aqueous electrolyte

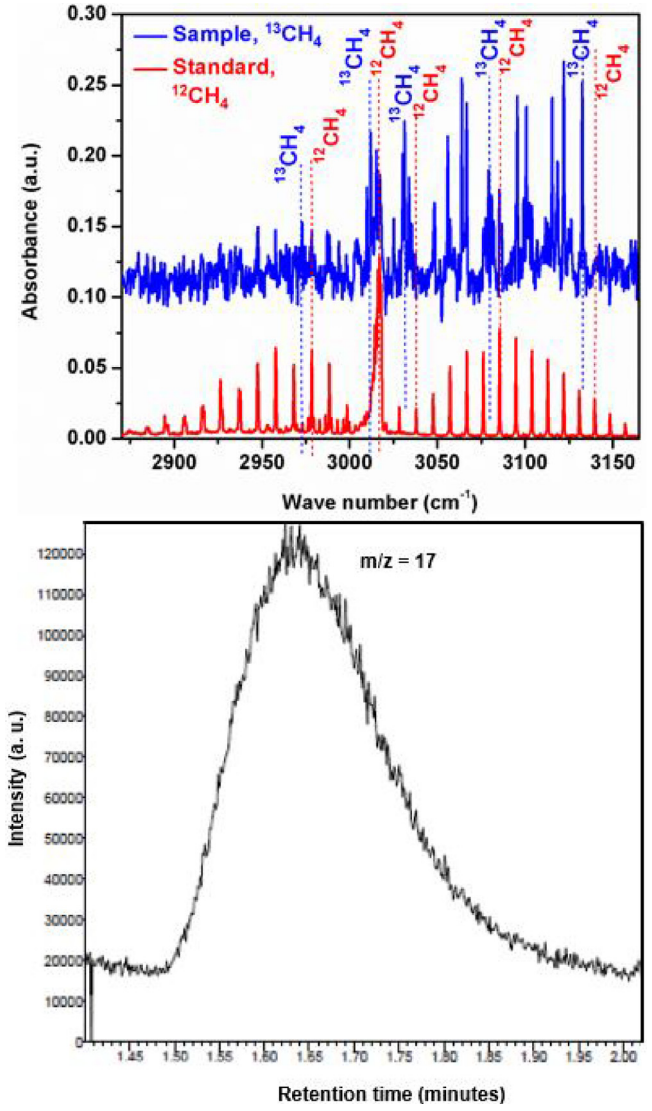

Fig. 8. (a) FTIR spectra of gas sample generated by photoreduction of $^{13}CO_2$ using FANT-eg. Shifts to lower wavenumbers (between 7 and 10 cm^{-1}) of peaks in ν_3 bands of the gas sample, from $^{12}CH_4$ standard, confirms presence of $^{13}CH_4$ as a product. (b) GS–MS ion-chromatogram at m/z = 17, confirming presence of $^{13}CH_4$ by photoreduction of $^{13}CO_2$.

(LANT-aq and FANT-aq). Although the yield of CH_4 per unit mass was higher for FANT-aq, the CH_4 yield in terms of yield per unit area was higher for FANT-eg. While LANT-eg did not quite outperform LANT-aq in terms of the yield per unit area metric, the disparity between the two became much smaller.

While CH_4 is a major product of CO_2 reduction, we also observed CO and trace amounts of C_2H_4 and C_2H_6 in our GC–MS and GC-FID based gas analysis (Fig. S10 and S11). In addition to gas phase experiments, our liquid phase CO_2 reduction experiments (described in the Supporting Information, and Fig. S12), proved the absence of reaction intermediates such as CO_3^-, HCO_3^-, $HCOO^-$, *etc.* We also assessed re-usability/stability of catalysts, in which we found that FANT-aq and FANT-eg exhibited good stability, in that product yield (Fig S13, below) went down slightly and thereafter remained constant.

In order to confirm CH_4 formation from the photoreduction of CO_2 and to rule out any possibility of carbon contamination, we performed isotope labelling experiments using $^{13}CO_2$ instead of $^{12}CO_2$ under identical reaction conditions. GC–MS (Fig. 8b) and gas phase FTIR analysis (Fig. 8a) of the gas evolved in the photoreactor after exposure of FANT-eg to the LED source in the presence of $^{13}CO_2$ and water vapor, confirmed the presence of $^{13}CH_4$. The GC–MS spectra (Fig. 8b) of reaction products showed an ion-chromatogram peak at *m/e* value of 17 for $^{13}CH_4$, confirming that CH_4 was formed by photoreduction of CO_2. FTIR spectra (Fig. 8a) showed an isotope effect-induced shift in the C–H stretching mode from 3017 cm^{-1} in $^{12}CH_4$ to 3010 cm^{-1} indicative of the presence of $^{13}CH_4$ in the produced gas [92–94]. Similar peak shifts were observed for other IR active modes for $^{13}CH_4$, as shown in Fig. 8a. In addition to the isotope labelling study, we also performed a series of control experiments by: (i) exposing TiO_2 nanotubes in the reactor to light in presence of water droplets and CO_2 (without heat and therefore no water vapor); (ii) placing TiO_2 nanotubes in the reactor filled with CO_2 and water vapor only, without illumination (to verify the action of light); (iii) not using TiO_2 (or any catalyst), but exposing the reactor to light, with water vapor and CO_2 in it (to detect any methane impurities in the reactor); (iv) not using TiO_2 (or any catalyst) and water vapor, but by exposing the reactor with CO_2 to light and heat (to detect any methanation of carbon impurities in reactor); and (v) by exposing TiO_2 nanotubes in the reactor to light, with the reactor having water vapor but no CO_2 (to verify that CO_2 is an essential reactant for methane generation). In each of these control experiments, the CH_4 yield was negligibly low, implying that CH_4 was produced by CO_2 photoreduction in the presence of catalyst, water vapor (produced by heating), light and CO_2. In experiments with only heat and no light, with FANT-eg, CH_4 produced was explicitly low and the obtained CH_4 yield was subtracted from the total CH_4 yield, to calculate the total quantity of CH_4 produced in experiments with heat and light.

3.3. Interaction of incident light with regular- and flame annealed TiO_2 nanotubes

A key question that arises is what effects relevant to photocatalytic action result from the differences in the structures and morphologies of the flame annealed titania nanotubes *vs* the regular furnace annealed nanotubes. One critical effect that is morphology and phase-dependent is the propagation of light and the concomitant spatial distribution of the electric field intensity in the photocatalysts. In order to investigate the effect of nanotube shape and phase content, we used Lumerical® to simulate the optical properties of the nanotubes, and the results are shown in Fig. 9 and in Fig. S8 in Supporting Information.

Fig. 9 indicates that the propagation of light is different in the LANT and FANT-eg samples. Areas with high local electric fields (hot spots) are particularly beneficial in photocatalysis. Since the nanotubes exhibited a peak visible light response at a wavelength of 450 nm as seen in Fig. S7, the Poynting vector plots of LANT and FANT-eg were examined at this wavelength in the substrate plane. In Fig. 9a (LANT), hot spots are found on the outer surface of the nanotubes alone while in Fig. 9b (FANT-eg), hot spots are found on both the inner and outer surfaces of the nanotubes. The electric field intensities were examined at the optical band edge (400 nm) in the plane orthogonal to both the substrate and the optical polarization (Figs. 9c and d). In Fig. 9c, the extinction of the electric field due to absorption of incident 450 nm light in the nanotubes with circular cross-section is not complete as is evident from the higher field intensities observed close to the bottom of the nanotubes. On the other hand, more complete absorption of incident light is observed in the square nanotubes (Fig. 9d). The utilization of photons at the semiconductor band-edge is a loss mechanism in all solar energy harvesting devices, and our simulations demonstrate that square-shaped, mixed phase nanotubes (FANT-eg) absorb 400 nm band-edge photons more effectively than anatase phase nanotubes with a circular cross-section (LANT), and also result in a larger number of hot spots when irradiated with visible light.

Fig. S9 (Supporting Information) shows the simulated absorption and scattering efficiency spectra for single nanotubes of the three different types investigated in this study. LANT-type nanotubes exhibit a strong scattering peak at a wavelength slightly lower than 400 nm (Fig. 98a) which manifests itself in the experimentally observed UV–vis

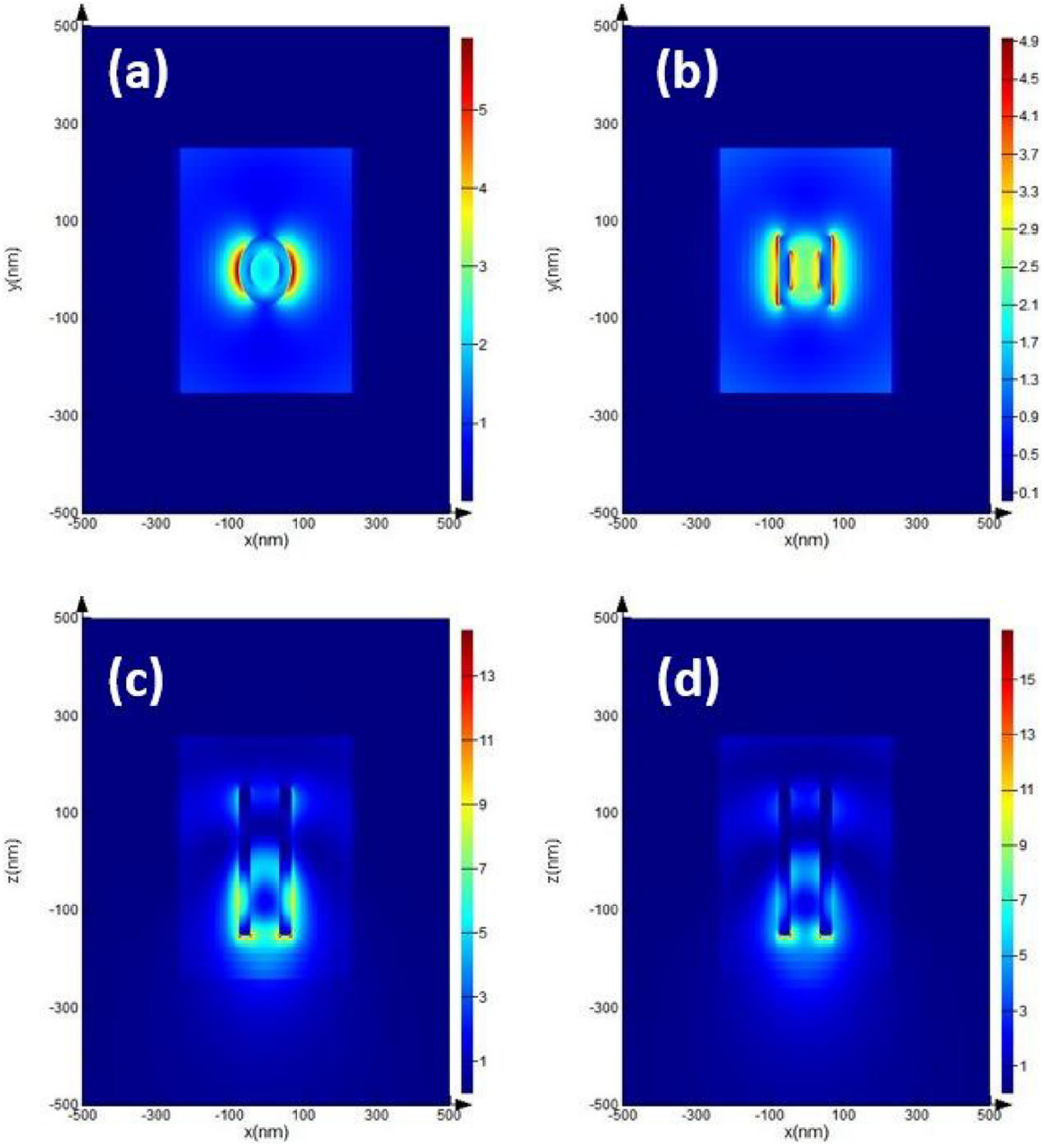

Fig. 9. Poynting vector plots for (a) LANT and (b) FANT-eg for λ = 450 nm. Electric field intensity plots for (c) LANT and (d) FANT-eg for λ = 400 nm.

spectrum of the LANT sample (black curve in Fig. 6) as a strong dip in absorption at a wavelength slightly lower than 400 nm. Similarly, the strong scattering peak of FANT-eg type nanotubes seen in Fig. S9b at a wavelength slightly higher than 400 nm manifests itself in the experimentally observed UV–vis spectrum of the FANT-eg sample (cyan curve in Fig. 6) as a strong dip in absorption at a wavelength slightly higher than 400 nm. Our simulations indicate that FANT-aq type nanotubes exhibit a broad, multi-peaked scattering feature in the 400–700 nm spectral range (Fig. S9c), which corresponds well with the large trough in the 400–700 nm spectral range in the experimentally observed UV–vis spectrum of the FANT-aq sample (red curve in Fig. 6). It must be noted though, that the effects of Ti^{3+} states and free electrons on the absorption of the samples were not incorporated into the model used to simulate the optical properties of the nanotubes.

3.4. Mechanism of CO_2 reduction

In general, the photoreduction of CO_2 by one electron—which forms a bent $CO_2^{\bullet -}$ anion radical—is highly unfavorable due to repulsion between *p* orbitals, which necessitates a high reduction potential (–1.90 V). However, proton assisted reduction of CO_2 by multiple electrons and protons proceeds at lower applied reduction potentials. CH_4 formation from CO_2 by 8 electrons and 8 protons needs only –0.24 V (*vs* NHE at pH-7). For the sustainable supply of electrons and protons, water must be oxidized to oxygen along with generation of electrons and protons needed for the photoreduction of CO_2. Therefore, for efficient CO_2 photoreduction to methane, the position of the conduction band of the photocatalyst must be more negative than reduction potential of CO_2/CH_4 (-0.24 V *vs* NHE at pH-7) whilst the position of the valence band should be more positive than the oxidation potential of water (H_2O/O_2 $+0.82$ V *vs* NHE at pH-7 or $+1.23$ V *vs* NHE at pH 0). Therefore, the bandgap of the semiconductor should be higher

than 1.23 eV in order to achieve CO_2 reduction *and* water splitting. Anatase phase of TiO_2 possesses a wide band gap of 3.2 eV with a conduction band position of −0.99 V *vs* NHE at pH-7 and valence band position of +2.10 V *vs* NHE at pH 7 [97,98]. The position of the conduction band of rutile TiO_2 is 0.2 V lower than of anatase form with a bandgap value of 3.0 eV. Annealing of TiO_2 in oxygen deficient conditions can induce oxygen vacancies and Ti^{3+} states, which create subenergy levels below the conduction band [99]. These subenergy levels decrease the energy required for the excitation of electrons which is evident from the UV–vis spectra in Fig. 6. For FANT-aq, flame annealing transforms anatase phase to pure rutile with a slightly lower band gap value (3.0 eV). The effective band gap is further reduced due to defects and subenergy levels, and therefore better light absorption characteristics and photocatalytic performance were observed with FANT-aq. However, for single phase rutile TiO_2, the carrier recombination is faster than for TiO_2 containing a mixture of anatase and rutile phases [52]. Loss of carriers to recombination is somewhat mitigated by the thin walls of the water anodized FANT-aq resulting in their enhanced CO_2 photoreduction performance. In addition to the above phenomenon, the preferentially oriented rutile (110) in FANT-aq is a likely facilitator of enhanced CH_4 yield because, in such crystalline planes, fast hydrogenation of activated CO_2 occurs *via* the carbene pathway [100]. In FANT-eg, both anatase and rutile phases are present and expected to enhance CH_4 yield due to reduced recombination of photogenerated carriers. Fig. 10 illustrates the mechanism with FANT-eg, where both rutile and anatase phase co-exist. The synergetic enhancement of photocatalytic activity due to the presence of both anatase and rutile is well documented [52,101,102]; the energy difference between conduction bands of anatase and rutile TiO_2 causes photogenerated electrons in the conduction band of anatase TiO_2 to be transferred to the conduction band of rutile in mixed phase TiO_2. There are, however, other literature reports that, on the basis of XPS, EPR and theoretical calculations, claim that anatase TiO_2 possesses low energy shallow traps (0.8 eV below the conduction band of rutile) that cause electrons to move from rutile to anatase as well [102–104]. Holes can remains in the valence band of the same semiconductor or can move to valence band of rutile or anatase TiO_2 depending on the type of transition and energy state. Either due to transfer of electrons from anatase to rutile or *vice versa*, efficient separation of charge carriers in mixed phase TiO_2 was achieved. Furthermore, the presence of sub-gap energy levels just below the conduction bands made lower energy transitions feasible under visible light irradiation.

$$TiO_2 \rightarrow TiO_2(h^+ + e^-) \quad (7)$$

$$H_2O + h^+ \rightarrow H^+ + {}^*OH \quad (8)$$

$$H^+ + e^- \rightarrow H_* \quad (9)$$

$$CO_2 \xrightarrow{e^-} {}^\bullet CO_{2*}^- \xrightarrow{H_*} CO + OH^- \xrightarrow{e^-} {}^\bullet CO^- \xrightarrow{H_*} C_* + OH^- \xrightarrow{e^-} {}^\bullet CH_* \xrightarrow{H_*} CH_{2*} \xrightarrow{H_*} {}^\bullet CH_{3*} \xrightarrow{H_*} CH_4 \quad (10)$$

The photoreduction in the presence of water vapor and CO_2 likely initiates by adsorption of the reactants (CO_2 and H_2O) on the TiO_2 surface followed by photo-induced activation by electron and hole transfer, respectively [90,105]. Illumination creates charge carriers, the carriers are separated owing to the nanotube morphology (wall-thickness ~ carrier diffusion length), the holes in the valence band of TiO_2 dissociate water to protons and OH- (which get converted into oxygen) (Eqs. (7)–(10)). The protons, after accepting one electron from the conduction band, get transformed to atomic hydrogen (H^*), while the adsorbed CO_2 gets activated to $CO_2^{\bullet -}$ through electron transfer from TiO_2. The high majority carrier concentration in TiO_2 nanotubes (particularly those formed in EG electrolyte) indicated by the monotonically increasing Drude electron absorption in Fig. 6 is known to facilitate electron transfer and improve photocatalytic performance [106]. Through subsequent steps involving activated $CO_2{}^\bullet-$ and multiple H^*, CH_4 was formed as the final product. The transformation of CO_2 into CH_4 follows three pathways *i.e.* carbene pathway, formaldehyde pathway and carboxylate pathway [107,108]. Based on previous EPR

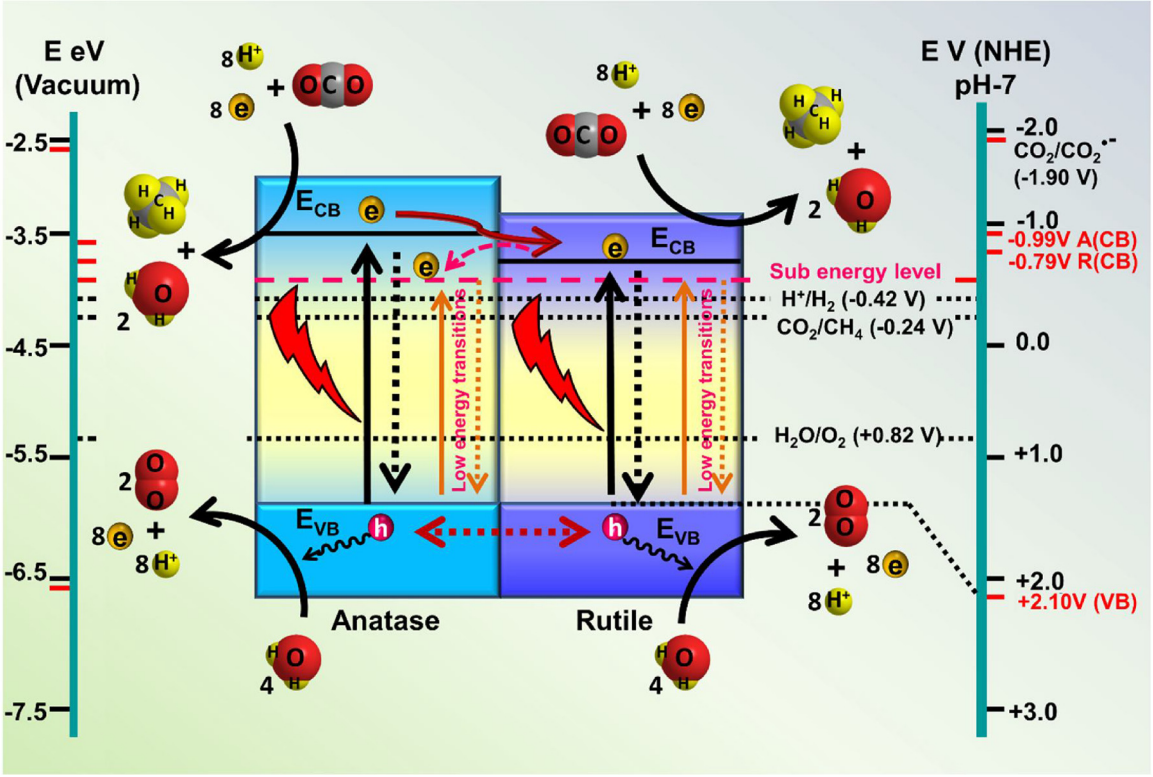

Fig. 10. Plausible mechanism of photoreduction of CO_2 by mixed phase FANT-eg nanotubes. The mechanism is arrived at by closely considering pertinent reactions and material properties reported in the literature [98,103,113].

studies [109,110], the methanation of CO_2 by the carbene pathway in the presence of H^* atoms and Ti^{3+} defects proceeds by formation of active surface carbon (*i.e.* C_*), which is converted into CH_4 as depicted in the reaction given in Eq. (10). As evident from Eq. (10), by-products such as formaldehyde, methanol and carboxylates (CO_3^-, HCO_3^-, $HCOO^-$, *etc.*) are absent [98,108–112] leading to the more selective formation of CH_4. This was confirmed by HPLC (Fig. S12) which failed to detect formaldehyde or formic acid in the reaction products. On the other hand, isotope labeled gas chromatography-mass spectrometry (GC−MS) confirmed the presence of ^{13}CO following the photoreduction of $^{13}CO_2$. Since CO is a key reaction intermediate in Eq. (10), the detection of CO (Fig. S10) strongly supports the carbene pathway as the mechanistic route for CO_2 photoreduction in our samples. The absence of any detectable H_2 can be explained from the less negative reduction potential of CO_2/CH_4 (–0.24 V *vs* NHE at pH 7) in comparison to H^+/H_2 (–0.42 V *vs* NHE at pH 7), which promotes formation of the more thermodynamically stable CH_4 as the product. Furthermore, the excess of CO_2 in reaction mixture ruled out possible recombination of H^* to form H_2.

4. Conclusion

Carbon dioxide was photocatalytically transformed into light hydrocarbons using flame annealed TiO_2 nanotubes with methane as the dominant hydrocarbon product and ethane and ethylene as minor products. The CH_4 yields for CO_2 photoreduction using high temperature flame annealed TiO_2 nanotubes are amongst the highest reported for bare TiO_2 nanotubes, and are either comparable to or exceed CH_4 yields obtained with TiO_2-based functionalized catalysts and nanocomposites. Isotope labelling experiments performed using GC−MS and gas phase FTIR provided confirmation that the CH_4 is produced by CO_2 photoreduction, and not due to either adventitious carbon or carbon introduced into the nanotubes during the anodic synthesis or the flame annealing treatment. The flame annealed nanotubes exhibited significant photoactivity for CO_2 reduction under visible light irradiation with a peak response at 450 nm and a photocatalytic activity edge that extended to photon energies as low as 2 eV. The visible light activity was attributed to defect-mediated absorption from localized Ti^{3+} states. Given the composition and band-edges of the TiO_2 nanomaterials employed in this study, the carbene pathway is the most likely reaction mechanism for the sunlight driven transformation of CO_2 into methane. In this work, we also generated experimental support for the carbene pathway through the detection of the presence of CO and the absence of HCHO and HCOOH in the product mixture. Square shaped flame annealed nanotubes were found to interact with light in a slightly different manner from regular nanotubes with circular cross-sections, exhibiting a higher density of electromagnetic hot spots for visible light and stronger absorption of ultraviolet photons. Flame annealing partially transformed anatase phase into the more thermodynamically stable rutile phase in ethylene glycol based TiO_2 nanotubes, which in turn, created a favorable band alignment inside the nanotubes enabling charge carrier separation and promoting photocatalytic activity, which resulted in enhanced CO_2 photoreduction to CH_4.

Conflicts of Interest

The authors have no conflicts to declare.

Acknowledgements

All authors thank NSERC, NRC-NINT, CFI, CMC Microsystems and Future Energy Systems for financial support. U.K.T. acknowledges Alberta Innovates Technology Futures for scholarship support. The characterization assistance provided by Dr. Kai Cui (NRC-NINT), Dr. Wayne Moffat (UofA), Ms. Lisa Nikolai, and the staff at the UofA Nanofab is acknowledged. P.K. and K.S offer their heartfelt thanks to Prof. Arvind Rajendran, Libardo Perez and James Sawada for generous assistance with gas chromatography.

Appendix A. Supplementary data

Supplementary material related to this article can be found, in the online version, at doi:https://doi.org/10.1016/j.apcatb.2018.08.002.

References

[1] S.T. Henriques, K.J. Borowiecki, The drivers of long-run CO_2 emissions in Europe, North America and Japan since 1800, Energy Policy 101 (2017) 537–549.
[2] S.A. Rackley, Carbon Capture and Storage, Butterworth-Heinemann, Oxford (U.K.), 2017.
[3] A.W. Kleij, M. North, A. Urakawa, CO_2 catalysis, ChemSusChem 10 (2017) 1036–1038.
[4] N. Hicks, U. Vik, P. Taylor, E. Ladoukakis, J. Park, F. Kolisis, K.S. Jakobsen, Using prokaryotes for carbon capture storage, Trends Biotechnol. 35 (2017) 22–32.
[5] M. Halmann, Photoelectrochemical reduction of aqueous carbon dioxide on *p*-type gallium phosphide in liquid junction solar cells, Nature 275 (1978) 115.
[6] B. Aurian-Blajeni, M. Halmann, J. Manassen, Photoreduction of carbon dioxide and water into formaldehyde and methanol on semiconductor materials, Sol. Energy 25 (1980) 165–170.
[7] S. Navalón, A. Dhakshinamoorthy, M. Álvaro, H. Garcia, Photocatalytic CO_2 reduction using non-titanium metal oxides and sulfides, ChemSusChem 6 (2013) 562–577.
[8] Z. Sheng, P. Kar, U.K. Thakur, K. Shankar, A review on photocatalytic CO_2 reduction using perovskite oxide nanomaterials, Nanotechnology 29 (5) (2018) 052001.
[9] S.U.M. Khan, M. Al-Shahry, W.B. Ingler, Efficient photochemical water splitting by a chemically modified n-TiO_2, Science 297 (2002) 2243.
[10] K. Shankar, M. Paulose, G.K. Mor, O.K. Varghese, C.A. Grimes, A study on the spectral photoresponse and photoelectrochemical properties of flame-annealed titania nanotube-arrays, J. Phys. D Appl. Phys. 38 (2005) 3543.
[11] K.S. Raja, M. Misra, V.K. Mahajan, T. Gandhi, P. Pillai, S.K. Mohapatra, Photoelectrochemical hydrogen generation using band-gap modified nanotubular titanium oxide in solar light, J. Power Sources 161 (2006) 1450–1457.
[12] R. Hahn, A. Ghicov, J. Salonen, V.-P. Lehto, P. Schmuki, Carbon doping of self-organized TiO_2 nanotube layers by thermal acetylene treatment, Nanotechnology 18 (2007) 105604.
[13] C. Xu, Y.A. Shaban, W.B. Ingler, S.U.M. Khan, Nanotube enhanced photoresponse of carbon modified (CM)-n-$TiO_2$for efficient water splitting, Sol. Energy Mater. Sol. Cells 91 (2007) 938–943.
[14] A.B. Murphy, Does carbon doping of TiO_2 allow water splitting in visible light? Comments on “Nanotube enhanced photoresponse of carbon modified (CM)-n-TiO_2 for efficient water splitting, Sol. Energy Mater. Sol. Cells 92 (2008) 363–367.
[15] X. Chen, L. Liu, Y.Y. Peter, S.S. Mao, Increasing solar absorption for photocatalysis with black hydrogenated titanium dioxide nanocrystals, Science 331 (2011) 746–750.
[16] G. Wang, H. Wang, Y. Ling, Y. Tang, X. Yang, R.C. Fitzmorris, C. Wang, J.Z. Zhang, Y. Li, Hydrogen-treated TiO_2 nanowire arrays for photoelectrochemical water splitting, Nano Lett. 11 (2011) 3026–3033.
[17] A. Naldoni, M. Allieta, S. Santangelo, M. Marelli, F. Fabbri, S. Cappelli, C.L. Bianchi, R. Psaro, V. Dal Santo, Effect of nature and location of defects on bandgap narrowing in black TiO_2 nanoparticles, J. Am. Chem. Soc. 134 (2012) 7600–7603.
[18] W. Zhou, W. Li, J.-Q. Wang, Y. Qu, Y. Yang, Y. Xie, K. Zhang, L. Wang, H. Fu, D. Zhao, Ordered mesoporous black TiO_2 as highly efficient hydrogen evolution photocatalyst, J. Am. Chem. Soc. 136 (2014) 9280–9283.
[19] N. Liu, C. Schneider, D. Freitag, M. Hartmann, U. Venkatesan, J. Müller, E. Spiecker, P. Schmuki, Black TiO_2 nanotubes: cocatalyst-free open-circuit hydrogen generation, Nano Lett. 14 (2014) 3309–3313.
[20] M. Tian, M. Mahjouri-Samani, G. Eres, R. Sachan, M. Yoon, M.F. Chisholm, K. Wang, A.A. Puretzky, C.M. Rouleau, D.B. Geohegan, G. Duscher, Structure and formation mechanism of black TiO2 nanoparticles, ACS Nano 9 (2015) 10482–10488.
[21] K. Shankar, J.I. Basham, N.K. Allam, O.K. Varghese, G.K. Mor, X. Feng, M. Paulose, J.A. Seabold, K.-S. Choi, C.A. Grimes, Recent advances in the use of TiO2 nanotube and nanowire arrays for oxidative photoelectrochemistry, J. Phys. Chem. C 113 (2009) 6327–6359.
[22] N.T. Nguyen, M. Altomare, J.E. Yoo, N. Taccardi, P. Schmuki, Noble metals on anodic TiO_2 nanotube mouths: thermal dewetting of minimal Pt Co-catalyst loading leads to significantly enhanced photocatalytic H_2 generation, Adv. Energ. Mater. 6 (2016) 1501926.
[23] P. Kar, Y. Zhang, S. Farsinezhad, A. Mohammadpour, B.D. Wiltshire, H. Sharma, K. Shankar, Rutile phase n-and p-type anodic titania nanotube arrays with square-shaped pore morphologies, Chem. Commun. 51 (37) (2015) 7816–7819.
[24] S. Kurian, H. Seo, H. Jeon, Significant enhancement in visible light absorption of TiO_2 nanotube arrays by surface band gap tuning, J. Phys. Chem. C 117 (2013) 16811–16819.
[25] K. Shankar, G.K. Mor, A. Fitzgerald, C.A. Grimes, Cation effect on the electrochemical formation of very high aspect ratio TiO_2 nanotube arrays in formamide – Water mixtures, J. Phys. Chem. C 111 (2007) 21–26.

[26] O.K. Varghese, D. Gong, M. Paulose, K.G. Ong, E.C. Dickey, C.A. Grimes, Extreme changes in the electrical resistance of titania nanotubes with hydrogen exposure, Adv. Mater. 15 (2003) 624–627.

[27] J. Zou, Q. Zhang, K. Huang, N. Marzari, Ultraviolet photodetectors based on anodic TiO_2 nanotube arrays, J. Phys. Chem. C 114 (2010) 10725–10729.

[28] M.H. Zarifi, A. Mohammadpour, S. Farsinezhad, B.D. Wiltshire, M. Nosrati, A.M. Askar, M. Daneshmand, K. Shankar, Time-resolved microwave photoconductivity (TRMC) using planar microwave resonators: application to the study of long-lived charge pairs in photoexcited titania nanotube arrays, J. Phys. Chem. C 119 (2015) 14358–14365.

[29] H. Cui, W. Zhao, C. Yang, H. Yin, T. Lin, Y. Shan, Y. Xie, H. Gu, F. Huang, Black TiO_2 nanotube arrays for high-efficiency photoelectrochemical water-splitting, J. Mater. Chem. A Mater. Energy Sustain. 2 (2014) 8612–8616.

[30] G.K. Mor, K. Shankar, M. Paulose, O.K. Varghese, C.A. Grimes, Enhanced photocleavage of water using titania nanotube arrays, Nano Lett. 5 (2005) 191–195.

[31] W.-N. Wang, W.-J. An, B. Ramalingam, S. Mukherjee, D.M. Niedzwiedzki, S. Gangopadhyay, P. Biswas, Size and structure matter: enhanced CO2 photoreduction efficiency by size-resolved ultrafine Pt nanoparticles on TiO2 single crystals, J. Am. Chem. Soc. 134 (2012) 11276–11281.

[32] X. Zhang, F. Han, B. Shi, S. Farsinezhad, G.P. Dechaine, K. Shankar, Photocatalytic conversion of diluted CO_2 into light hydrocarbons using periodically modulated multiwalled nanotube arrays, Angew. Chem. 124 (2012) 12904–12907.

[33] Osamu Ishitani, C. Inoue, Y. Suzuki, T. Ibusuki, Photocatalytic reduction of carbon dioxide to methane and acetic acid by an aqueous suspension of metal-deposited TiO_2, J. Photochem. Photobiol. A Chem. 72 (1993) 269–271.

[34] Ş. Neaţu, J.A. Maciá-Agulló, P. Concepción, H. Garcia, Gold–Copper nanoalloys supported on TiO2 as photocatalysts for CO2 reduction by water, J. Am. Chem. Soc. 136 (2014) 15969–15976.

[35] S. Farsinezhad, H. Sharma, K. Shankar, Interfacial band alignment for photocatalytic charge separation in TiO_2 nanotube arrays coated with CuPt nanoparticles, Phys. Chem. Chem. Phys. 17 (2015) 29723–29733.

[36] P. Kar, S. Farsinezhad, N. Mahdi, Y. Zhang, U. Obuekwe, H. Sharma, J. Shen, N. Semagina, K. Shankar, Enhanced CH_4 yield by photocatalytic CO_2 reduction using TiO_2 nanotube arrays grafted with Au, Ru, and ZnPd nanoparticles, Nano Res. 9 (2016) 3478–3493.

[37] J. Jiao, Y. Wei, Y. Zhao, Z. Zhao, A. Duan, J. Liu, Y. Pang, J. Li, G. Jiang, Y. Wang, AuPd/3DOM-TiO_2 catalysts for photocatalytic reduction of CO2: high efficient separation of photogenerated charge carriers, Appl. Catal. B-Environ. 209 (2017) 228–239.

[38] M. Tahir, B. Tahir, N.A.S. Amin, Synergistic effect in plasmonic Au/Ag alloy NPs co-coated TiO_2 NWs toward visible-light enhanced CO_2 photoreduction to fuels, Appl. Catal. B-Environ. 204 (2017) 548–560.

[39] F. Zhou, H. Li, M. Fournier, D.R. MacFarlane, Electrocatalytic CO_2 reduction to formate at Low Overpotentials on electrodeposited Pd films: stabilized performance by suppression of CO formation, ChemSusChem 10 (2017) 1509–1516.

[40] Z. Zhao, Z. Chen, G. Lu, Computational discovery of nickel-based catalysts for CO_2 reduction to formic acid, J. Phys. Chem. C 121 (2017) 20865–20870.

[41] P. Kar, S. Farsinezhad, X. Zhang, K. Shankar, Anodic Cu_2S and CuS nanorod and nanowall arrays: preparation, properties and application in CO_2 photoreduction, Nanoscale 6 (2014) 14305–14318.

[42] S. Thomas, K. Stefanie, P. Kristin, P. Oliver, D. Kay, F. Daniel, O. Ivan, S. Adriana, K. Ernst-Bernhard, T. Andreas, Materials pushing the application limits of wire grid polarizers further into the deep ultraviolet spectral range, Adv. Opt. Mater. 4 (2016) 1780–1786.

[43] Y. Zhang, S. Farsinezhad, B.D. Wiltshire, R. Kisslinger, P. Kar, K. Shankar, Optical anisotropy in vertically oriented TiO_2 nanotube arrays, Nanotechnology 28 (2017) 374001.

[44] K. Shankar, G.K. Mor, H.E. Prakasam, S. Yoriya, M. Paulose, O.K. Varghese, C.A. Grimes, Highly-ordered TiO_2 nanotube arrays up to 220 μm in length: use in water photoelectrolysis and dye-sensitized solar cells, Nanotechnology 18 (2007) 065707.

[45] S. Farsinezhad, P.R. Waghmare, B.D. Wiltshire, H. Sharma, S. Amiri, S.K. Mitra, K. Shankar, Amphiphobic surfaces from functionalized TiO_2 nanotube arrays, RSC Adv. 4 (2014) 33587–33598.

[46] M.A. Khan, H.-T. Jung, O.-B. Yang, Synthesis and characterization of ultrahigh crystalline TiO_2 nanotubes, J. Phys. Chem. B 110 (2006) 6626–6630.

[47] M.-J. López-Muñoz, A. Arencibia, L. Cerro, R. Pascual, Á. Melgar, Adsorption of Hg (II) from aqueous solutions using TiO_2 and titanate nanotube adsorbents, Appl. Surf. Sci. 367 (2016) 91–100.

[48] Y. Sun, K. Yan, G. Wang, W. Guo, T. Ma, Effect of annealing temperature on the hydrogen production of TiO_2 nanotube arrays in a two-compartment photoelectrochemical cell, J. Phys. Chem. C 115 (2011) 12844–12849.

[49] M. Jarosz, K. Syrek, J. Kapusta-Kołodziej, J. Mech, K. Małek, K. Hnida, T. Łojewski, M. Jaskuła, G.D. Sulka, Heat treatment effect on crystalline structure and photoelectrochemical properties of anodic TiO_2 nanotube arrays formed in ethylene glycol and glycerol based electrolytes, J. Phys. Chem. C 119 (2015) 24182–24191.

[50] W. Li, C. Ni, H. Lin, C. Huang, S.I. Shah, Size dependence of thermal stability of TiO_2 nanoparticles, J. Appl. Phys. 96 (2004) 6663–6668.

[51] H. Nakajima, T. Mori, Q. Shen, T. Toyoda, Photoluminescence study of mixtures of anatase and rutile TiO_2 nanoparticles: influence of charge transfer between the nanoparticles on their photoluminescence excitation bands, Chem. Phys. Lett. 409 (2005) 81–84.

[52] R. Su, R. Bechstein, L. Sø, R.T. Vang, M. Sillassen, B. Esbjornsson, A. Palmqvist, F. Besenbacher, How the anatase-to-rutile ratio influences the photoreactivity of TiO_2, J. Phys. Chem. C 115 (2011) 24287–24292.

[53] W. Su, J. Zhang, Z. Feng, T. Chen, P. Ying, C. Li, Surface phases of TiO_2 nanoparticles studied by UV Raman spectroscopy and FT-IR spectroscopy, J. Phys. Chem. C 112 (2008) 7710–7716.

[54] J.-G. Li, T. Ishigaki, X. Sun, Anatase, brookite, and rutile nanocrystals via redox reactions under mild hydrothermal conditions: phase-selective synthesis and physicochemical properties, J. Phys. Chem. C 111 (2007) 4969–4976.

[55] A.S. Attar, Z. Hassani, Fabrication and growth mechanism of single-crystalline rutile TiO_2 nanowires by liquid-phase deposition process in a porous alumina template, J. Mater. Sci. Technol. 31 (2015) 828–833.

[56] B. Di Bartolo, Optical Interactions in Solids, World Scientific Publishing Company, 2010.

[57] Z. Pei, L. Ding, H. Lin, S. Weng, Z. Zheng, Y. Hou, P. Liu, Facile synthesis of defect-mediated TiO_{2-x} with enhanced visible light photocatalytic activity, J. Mater. Chem. A 1 (2013) 10099–10102.

[58] F. Zuo, L. Wang, T. Wu, Z. Zhang, D. Borchardt, P. Feng, Self-doped Ti^{3+} enhanced photocatalyst for hydrogen production under visible light, J. Am. Chem. Soc. 132 (2010) 11856–11857.

[59] C. Di Valentin, A. Selloni, Bulk and surface polarons in photoexcited anatase TiO_2, J. Phys. Chem. Lett. 2 (2011) 2223–2228.

[60] P. Johnson, R. Christy, Optical constants of transition metals: Ti, V, Cr, Mn, Fe, Co, Ni, and Pd, Phys. Rev. B 9 (1974) 5056.

[61] T. Berger, J.A. Anta, Vc. Morales-Flórez, Electrons in the band gap: spectroscopic characterization of anatase TiO_2 nanocrystal electrodes under fermi level control, J. Phys. Chem. C 116 (2012) 11444–11455.

[62] Z. Wang, B. Wen, Q. Hao, L.-M. Liu, C. Zhou, X. Mao, X. Lang, W.-J. Yin, D. Dai, A. Selloni, X. Yang, Localized excitation of Ti3 + ions in the photoabsorption and photocatalytic activity of reduced rutile TiO_2, J. Am. Chem. Soc. 137 (2015) 9146–9152.

[63] M. Paulose, K. Shankar, S. Yoriya, H.E. Prakasam, O.K. Varghese, G.K. Mor, T.A. Latempa, A. Fitzgerald, C.A. Grimes, Anodic growth of highly ordered TiO_2 nanotube arrays to 134 μm in length, J. Phys. Chem. B 110 (2006) 16179–16184.

[64] C. Di Valentin, G. Pacchioni, A. Selloni, Reduced and n-type doped TiO_2: nature of Ti^{3+} species, J. Phys. Chem. C 113 (2009) 20543–20552.

[65] M. Rajabi, S. Shogh, Defect study of TiO_2 nanorods grown by a hydrothermal method through photoluminescence spectroscopy, J. Lumin. 157 (2015) 235–242.

[66] Y. Chen, W. Li, J. Wang, Y. Gan, L. Liu, M. Ju, Microwave-assisted ionic liquid synthesis of Ti^{3+} self-doped TiO_2 hollow nanocrystals with enhanced visible-light photoactivity, Appl. Catal. B-Environ. 191 (2016) 94–105.

[67] Y. Zhou, C. Chen, N. Wang, Y. Li, H. Ding, Stable Ti^{3+} self-doped anatase-rutile mixed TiO_2 with enhanced visible light utilization and durability, J. Phys. Chem. C 120 (2016) 6116–6124.

[68] J. Chen, W. Song, H. Hou, Y. Zhang, M. Jing, X. Jia, X. Ji, Ti^{3+} self-doped dark rutile TiO_2 ultrafine nanorods with durable high-rate capability for lithium-ion batteries, Adv. Funct. Mater. 25 (2015) 6793–6801.

[69] Y. Yang, P. Gao, X. Ren, L. Sha, P. Yang, J. Zhang, Y. Chen, L. Yang, Massive Ti^{3+} self-doped by the injected electrons from external Pt and the efficient photocatalytic hydrogen production under visible-Light, Appl. Catal. B-Environ. 218 (2017) 751–757.

[70] L. Liu, Y. Jiang, H. Zhao, J. Chen, J. Cheng, K. Yang, Y. Li, Engineering coexposed {001} and {101} facets in oxygen-deficient TiO2 nanocrystals for enhanced CO2 photoreduction under visible light, ACS Catal. 6 (2016) 1097–1108.

[71] C. Mao, F. Zuo, Y. Hou, X. Bu, P. Feng, In situ preparation of a Ti^{3+} self-doped TiO_2 film with enhanced activity as photoanode by N_2H_4 reduction, Angew. Chem., Int. Ed. 53 (2014) 10485–10489.

[72] Z. Lian, W. Wang, G. Li, F. Tian, K.S. Schanze, H. Li, Pt-enhanced mesoporous Ti^{3+}/TiO_2 with rapid bulk to surface Electron transfer for photocatalytic hydrogen evolution, ACS Appl. Mater. Inter. 9 (2017) 16959–16966.

[73] R. Kumar, S. Govindarajan, R.K. Siri Kiran Janardhana, T.N. Rao, S.V. Joshi, S. Anandan, Facile one-step route for the development of in situ cocatalyst-modified Ti^{3+} self-doped TiO_2 for improved visible-light photocatalytic activity, ACS Appl. Mater. Inter. 8 (2016) 27642–27653.

[74] B. Jiang, Y. Tang, Y. Qu, J.-Q. Wang, Y. Xie, C. Tian, W. Zhou, H. Fu, Thin carbon layer coated Ti^{3+}-TiO_2 nanocrystallites for visible-light driven photocatalysis, Nanoscale 7 (2015) 5035–5045.

[75] S. Hoang, S.P. Berglund, N.T. Hahn, A.J. Bard, C.B. Mullins, Enhancing visible light photo-oxidation of water with TiO_2 nanowire arrays via cotreatment with H_2 and NH_3: synergistic effects between Ti^{3+} and N, J. Am. Chem. Soc. 134 (2012) 3659–3662.

[76] C. Mao, F. Zuo, Y. Hou, X. Bu, P. Feng, In situ preparation of a Ti^{3+} self-doped TiO_2 film with enhanced activity as photoanode by N_2H_4 reduction, Angew. Chem. 126 (2014) 10653–10657.

[77] R.F. Howe, M. Gratzel, EPR observation of trapped electrons in colloidal titanium dioxide, J. Phys. Chem. 89 (1985) 4495–4499.

[78] L.R. Grabstanowicz, S. Gao, T. Li, R.M. Rickard, T. Rajh, D.-J. Liu, T. Xu, Facile oxidative conversion of TiH_2 to high-concentration Ti^{3+}-self-doped rutile TiO_2 with visible-light photoactivity, Inorg. Chem. 52 (2013) 3884–3890.

[79] M. Nishikawa, Y. Mitani, Y. Nosaka, Photocatalytic reaction mechanism of Fe(III)-Grafted TiO2 studied by means of ESR spectroscopy and chemiluminescence photometry, J. Phys. Chem. C 116 (2012) 14900–14907.

[80] C.-C. Chen, S.-H. Hu, Y.-P. Fu, Effects of surface hydroxyl group density on the photocatalytic activity of Fe^{3+}-doped TiO_2, J. Alloys compd. 632 (2015) 326–334.

[81] B. Fang, A. Bonakdarpour, K. Reilly, Y. Xing, F. Taghipour, D.P. Wilkinson, Large-scale synthesis of TiO_2 microspheres with hierarchical nanostructure for highly efficient photodriven reduction of CO_2 to CH_4, ACS Appl. Mater. Inter. 6 (2014) 15488–15498.

[82] Q. Zhai, S. Xie, W. Fan, Q. Zhang, Y. Wang, W. Deng, Y. Wang, Photocatalytic conversion of carbon dioxide with water into methane: platinum and copper (I)

oxide co-catalysts with a core–shell structure, Angew. Chem. 125 (2013) 5888–5891.
[83] T. Yui, A. Kan, C. Saitoh, K. Koike, T. Ibusuki, O. Ishitani, Photochemical reduction of CO_2 using TiO_2: effects of organic adsorbates on TiO_2 and deposition of Pd onto TiO_2, ACS Appl. Mater. Inter. 3 (2011) 2594–2600.
[84] B. Fang, Y. Xing, A. Bonakdarpour, S. Zhang, D.P. Wilkinson, Hierarchical CuO–TiO_2 hollow microspheres for highly efficient photodriven reduction of CO_2 to CH_4, ACS Sustain. Chem. Eng. 3 (2015) 2381–2388.
[85] M. Anpo, M. Takeuchi, The design and development of highly reactive titanium oxide photocatalysts operating under visible light irradiation, J. Catal. 216 (2003) 505–516.
[86] D. Luo, W. Ma, L. Wu, K. Nakata, CO_2 Reduction by Photocatalysis on TiO_2, Advanced solid catalysts for renewable energy production, IGI Global, 2018, pp. 268–299.
[87] G. Liu, N. Hoivik, K. Wang, H. Jakobsen, Engineering TiO_2 nanomaterials for CO_2 conversion/solar fuels, Sol. Energy Mater. Sol. Cells 105 (2012) 53–68.
[88] Z. Xiong, Y. Luo, Y. Zhao, J. Zhang, C. Zheng, J.C. Wu, Synthesis, characterization and enhanced photocatalytic CO_2 reduction activity of graphene supported TiO_2 nanocrystals with coexposed {001} and {101} facets, Phys. Chem. Chem. Phys. 18 (2016) 13186–13195.
[89] A. Dhakshinamoorthy, S. Navalon, A. Corma, H. Garcia, Photocatalytic CO_2 reduction by TiO_2 and related titanium containing solids, Synth. Lect. Energy Environ. Technol. Sci. Soc. 5 (2012) 9217–9233.
[90] St. Neaţu, J.A. Maciá-Agulló, P. Concepción, H. Garcia, Gold–copper nanoalloys supported on TiO_2 as photocatalysts for CO_2 reduction by water, J. Am. Chem. Soc. 136 (2014) 15969–15976.
[91] J. Yu, J. Low, W. Xiao, P. Zhou, M. Jaroniec, Enhanced photocatalytic CO_2-reduction activity of anatase TiO_2 by coexposed {001} and {101} facets, J. Am. Chem. Soc. 136 (2014) 8839–8842.
[92] D. Scarano, S. Bertarione, G. Spoto, A. Zecchina, C.O. Arean, FTIR spectroscopy of hydrogen, carbon monoxide, and methane adsorbed and co-adsorbed on zinc oxide, Thin Solid Films 400 (2001) 50–55.
[93] R.S. McDowell, The ν_3 infrared bands of $C^{12}H_4$ and $C^{13}H_4$, J. Mol. Spectrosc. 21 (1966) 280–290.
[94] S.W. Reeve, W.A. Burns, Rotational analysis of FTIR spectra from cigarette smoke, J. Chem. Educ. 81 (2004) 865–867.
[95] X.-H. Xia, Z.-J. Jia, Y. Yu, Y. Liang, Z. Wang, L.-L. Ma, Preparation of multi-walled carbon nanotube supported TiO_2 and its photocatalytic activity in the reduction of CO_2 with H_2O, Carbon 45 (2007) 717–721.
[96] K. Kočí, L. Obalová, L. Matějová, D. Plachá, Z. Lacný, J. Jirkovský, O. Šolcová, Effect of TiO_2 particle size on the photocatalytic reduction of CO_2, Appl. Catal. B-Environ. 89 (2009) 494–502.
[97] E.V. Kondratenko, G. Mul, J. Baltrusaitis, G.O. Larrazábal, J. Pérez-Ramírez, Status and perspectives of CO_2 conversion into fuels and chemicals by catalytic, photocatalytic and electrocatalytic processes, Synth. Lect. Energy Environ. Technol. Sci. Soc. 6 (2013) 3112–3135.
[98] S.N. Habisreutinger, L. Schmidt-Mende, J.K. Stolarczyk, Photocatalytic reduction of CO_2 on TiO_2 and other semiconductors, Angew. Chem., Int. Ed. 52 (2013) 7372–7408.
[99] M. Li, W. Hebenstreit, U. Diebold, A.M. Tyryshkin, M.K. Bowman, G.G. Dunham, M.A. Henderson, The influence of the bulk reduction state on the surface structure and morphology of rutile TiO_2 (110) single crystals, J. Phys. Chem. B 104 (2000) 4944–4950.
[100] W.-J. Yin, M. Krack, B. Wen, S.-Y. Ma, L.-M. Liu, CO_2 capture and conversion on rutile TiO_2 (110) in the water environment: insight by first-principles calculations, J. Phys. Chem. Lett. 6 (2015) 2538–2545.
[101] R.I. Bickley, T. Gonzalez-Carreno, J.S. Lees, L. Palmisano, R.J. Tilley, A structural investigation of titanium dioxide photocatalysts, J. Solid State Chem. 92 (1991) 178–190.
[102] D.C. Hurum, A.G. Agrios, K.A. Gray, T. Rajh, M.C. Thurnauer, Explaining the enhanced photocatalytic activity of Degussa P25 mixed-phase TiO_2 using EPR, J. Phys. Chem. B 107 (2003) 4545–4549.
[103] D.O. Scanlon, C.W. Dunnill, J. Buckeridge, S.A. Shevlin, A.J. Logsdail, S.M. Woodley, C.R.A. Catlow, M.J. Powell, R.G. Palgrave, I.P. Parkin, Band alignment of rutile and anatase TiO_2, Nat. Mater. 12 (2013) 798.
[104] S. Leytner, J.T. Hupp, Evaluation of the energetics of electron trap states at the nanocrystalline titanium dioxide/aqueous solution interface via time-resolved photoacoustic spectroscopy, Chem. Phys. Lett. 330 (2000) 231–236.
[105] Ş. Neaţu, J.A. Maciá-Agulló, H. Garcia, Solar light photocatalytic CO_2 reduction: general considerations and selected bench-mark photocatalysts, Int. J. Mol. Sci. 15 (2014) 5246–5262.
[106] F. Amano, M. Nakata, A. Yamamoto, T. Tanaka, Effect of Ti^{3+} ions and conduction band electrons on photocatalytic and photoelectrochemical activity of rutile titania for water oxidation, J. Phys. Chem. C 120 (2016) 6467–6474.
[107] L. Liu, Y. Li, Understanding the reaction mechanism of photocatalytic reduction of CO_2 with H_2O on TiO_2-based photocatalysts: a review, Aerosol Air Qual. Res. 14 (2014) 453–469.
[108] K. Rajalakshmi, V. Jeyalakshmi, K.R. Krishnamurthy, B. Viswanathan, Photocatalytic reduction of carbon dioxide by water on titania: role of photophysical and structural properties, Indian J. Chem. 51A (2012) 411–419.
[109] M. Anpo, H. Yamashita, Y. Ichihashi, S. Ehara, Photocatalytic reduction of CO_2 with H_2O on various titanium oxide catalysts, J. Electroanal. Chem. Lausanne (Lausanne) 396 (1995) 21–26.
[110] C.-C. Yang, Y.-H. Yu, B. van der Linden, J.C. Wu, G. Mul, Artificial photosynthesis over crystalline TiO_2-based catalysts: fact or fiction? J. Am. Chem. Soc. 132 (2010) 8398–8406.
[111] N.M. Dimitrijevic, B.K. Vijayan, O.G. Poluektov, T. Rajh, K.A. Gray, H. He, P. Zapol, Role of water and carbonates in photocatalytic transformation of CO_2 to CH_4 on titania, J. Am. Chem. Soc. 133 (2011) 3964–3971.
[112] L. Liu, H. Zhao, J.M. Andino, Y. Li, Photocatalytic CO_2 reduction with H_2O on TiO_2 nanocrystals: comparison of anatase, rutile, and brookite polymorphs and exploration of surface chemistry, ACS Catal. 2 (2012) 1817–1828.
[113] W.-K. Wang, J.-J. Chen, X. Zhang, Y.-X. Huang, W.-W. Li, H.-Q. Yu, Self-induced synthesis of phase-junction TiO_2 with a tailored rutile to anatase ratio below phase transition temperature, Sci. Rep.-UK 6 (2016) 20491.